

System Design and Testing of the Hominid Robot

Charlie

Daniel Kuehn

Robotics Innovation Center (RIC)

German Research Center for Artificial Intelligence (DFKI)

28359 Bremen, Germany

`daniel.kuehn@dfki.de`

Moritz Schilling

Robotics Group

University of Bremen — Faculty 3

28359 Bremen, Germany

`moritz.schilling@uni-bremen.de`

Tobias Stark

Robotics Group

University of Bremen — Faculty 3

28359 Bremen, Germany

`tobias.stark@uni-bremen.de`

Martin Zenzes

Robotics Innovation Center (RIC)

German Research Center for Artificial Intelligence (DFKI)

28359 Bremen, Germany

`martin.zenzes@dfki.de`

Frank Kirchner

Robotics Innovation Center (RIC)

German Research Center for Artificial Intelligence (DFKI)

Robotics Group — University of Bremen — Faculty 3

28359 Bremen, Germany

`frank.kirchner@dfki.de`

Abstract

Today's and future application scenarios for mobile robots deal with increased requirements regarding autonomy and flexibility in the locomotor system. To cope with these demands, a high sensor quantity and quality allows to perform robust locomotion. The authors present a hominid robotic system which is equipped with multi-point-contact feet and an active artificial spine to incorporate extended sensing and locomotion capabilities for walking robots. In the proposed robotic system, the front and rear part are connected via an actuated spinal

structure with six degrees of freedom. In order to increase the robustness of the system's locomotion in terms of traction and stability, a foot-like structure equipped with various sensors has been developed. Altogether the robot embodies more than 330 sensors. In terms of distributed local control, the structures feature their own local intelligence and are as autonomous as possible regarding sensing, sensor preprocessing, control, and communication. This allows the robot to respond to external disturbances with minor latency.

Within this paper, the proposed robotic system and its distributed and hierarchical control method are presented. For validation purposes of the electro-mechanical and software approach, the authors present results verified experimentally in different environments (in- and outdoor) with differing walking speeds on various substrates and in varying inclinations from -20° to 20° . The results show that the presented approach is viable and improves the flexibility of the locomotor system.

A hominid design was chosen in order to perform various types of locomotion. To demonstrate the entire functionality of the developed hardware, two different motion modes (quadrupedal and bipedal locomotion) are investigated. This also includes a stable transition from a four-legged posture to an upright posture and vice versa.

Abbreviations

DoF Degree of Freedom

IMU Inertia Measurement Unit

ZMP Zero Moment Point

LVDS Low Voltage Differential Signaling

CoSP Center of Support Polygon

CoM Center of Mass

CoG Center of Gravity

RoM Range of Motion

MPCF multi-point-contact feet

SPCF single-point-contact feet

MCU motion control unit

NDLCom Node-level Data Link Communication

MDAQ multiplexed data acquisition

ADC analog-to-digital converter

PCB printed circuit board

BLDC brushless direct current

PEP posterior extreme position

AEP anterior extreme position

1 Introduction

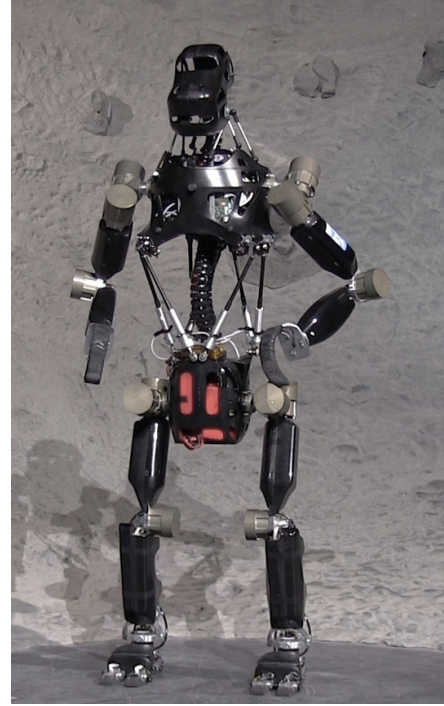
Possible areas of application for mobile robots have multiplied in the recent past. Nowadays, robotic systems have to deal more and more with increasingly challenging environments. In addition to search and rescue scenarios, human assistance, security, and especially exploration scenarios are covered topics. Robotic systems can provide certain services in these surroundings that would be too hazardous and too dangerous for humans. Besides protective applications, economic reasons cannot be denied since robots present themselves as economically viable alternatives.

Especially space exploration has become a major field of application for robotic systems. NASA recently stated that they found ice deposits close to the moon's north pole using imaging radar. To be more specific, the indication of water ice was found in more than 40 craters with a diameter range from one to nine miles, "which will give future missions a new target to further explore and exploit" (NASA.gov – Mini-RF, 2010). To investigate such discoveries, sending humans instead of robotic systems is more dangerous as well as more expensive. Even if humans are not replaced, robotic assistance can still be useful, e.g. building space habitats to create a permanent settlement for humans or, like Robonaut (Diftler et al., 2012), take over tasks which can become too dangerous or too monotonous for astronauts on the International Space Station (ISS).

In the recent past, rovers operated successful on other planets. Although wheeled or tracked vehicles have several advantages over stationary landers and are usually energy-efficient and easy to control, legged systems



(a) Charlie in a quadrupedal pose



(b) Charlie in a bipedal pose

Figure 1: Photographs of the presented hominid robot Charlie with its artificial spine and sensor feet in a four-legged and two-legged posture.

have access to a wider range of terrains as they are capable of applying forces in a noncontinuous way in innumerable directions and magnitudes within their designed workspace (Spenneberg and Kirchner, 2000). While this is useful for exploration scenarios in rough environments in which wheeled systems could get stuck, the robot can also be empowered to use its limbs beyond walking, e.g. for manipulation or sensing tasks. Especially in case of a humanoid appearance, it has the ability to linger within a workspace designed for humans (Bluethmann et al., 2003) and use the same tools. In this regard Stoica discusses the design criteria of robots which should assemble long-term habitats (Stoica et al., 2005).

This paper describes an ape-like robotic research platform named Charlie (see Fig. 1). It incorporates an active spine and feet with increased sensing capabilities which can improve the locomotion and mobility characteristics in rough terrain. The active spine connects the front and rear body and enables the hip and shoulder to be moved in all spatial directions and to rotate around all major axes. The robot's design is inspired by chimpanzees and allows the system performing quadrupedal and bipedal locomotion to meet different application areas.

As stated above, legged robots are able to provide a higher flexibility in their locomotion system than wheeled

or tracked vehicles. A variety of systems that mimic locomotion patterns of their natural counterpart have been successfully developed by a number of research groups such as the humanoid robot Asimo (Sakagami et al., 2002), the gecko-inspired stickyrobot (Hawkes et al., 2011), the fast running robot Cheetah (Briggs et al., 2012), the eight-legged robot Scorpion (Kirchner et al., 2002), or the robots designed in the MIT LegLab (Raibert, 1986), to name only a few. Csonka gives a brief history of legged robotics in (Csonka and Waldron, 2011). In the following some systems and concepts which are closely related to Charlie are presented.

Within the Charlie robot, the structures are as autonomous as possible regarding to sensing, sensor pre-processing, control, and communication. The structures feature an internal local processing unit, allowing the robots main processor to outsource certain control tasks. This is in opposition to a single, centralized controller, which has to deal with many different sensory inputs (e.g. more than 330 for Charlie) and motory outputs. In such a centralized architecture cabling, computational load balancing, and latencies are major issues. Charlie's structure is therefore based on a hierarchy of control loops which are distributed all over the robotic system. Distributed control proved to be useful in a wide range of different robotic systems, e.g. for insect-like hexapods (Espenschied et al., 1996) or for humanoid robots (Jantsch et al., 2010).

Force controlled multi-legged robots with single-point-contact feet like the Scorpion robot (Spenneberg and Kirchner, 2000) have shown their cross-country mobility. The usage of spherical shaped feet can be seen in four-legged robots like LittleDog (Murphy et al., 2011) and BigDog (Wooden et al., 2010) or in multi-legged systems like SpaceClimber (Bartsch et al., 2012). Spherical feet have the advantage to provide traction at any contact angle. Damping capabilities are not included in SpaceClimbers feet, but are realized in the lower thigh with a compliant degree of freedom. The four legged robot Starleth (Hutter et al., 2012) is close to Charlie regarding size and weight, but differs in sensory and electronic disposition as well as in the design of feet and spine.

The benefit of multi-point-contact feet (MPCF) is possibly not high for multi-legged robots, which have the intrinsic ability to generate a stable stance by selecting an appropriate walking pattern even with single-point-contact feet (SPCF). Consequently, for the sake of simplified design, weight, and control, most multi-legged systems neglect the foot issue. Considering the desire to receive various information from the feet, one gets more limited integrating sensors the smaller the structure is. In contrast, MPCF can have advantages for multi-legged locomotion as well, since a better adaptation to difficult terrain leads to increased traction. These kind of feet offer more space so multiple sensors can be included, which will be useful if, for example, proprioceptive information is used to detect different soils and adapt the walking pattern accordingly. In

addition, a MPCF offers the desired ability to let the robot walk on two legs, which would be difficult to realize with SPCF.

Hashimoto introduced a new foot design for a two-legged robot, where one spike-like structure is integrated in each corner of a rectangular-shaped foot (Hashimoto et al., 2006). The foot has one Degree of Freedom (DoF) in the ankle joint and adapts its four main contact points to compensate small irregularities of up to 2 cm. One drawback is that the function of this foot cannot be applied on deformable surfaces. Most bipedal robots like Asimo (Sakagami et al., 2002), WABIAN2 (Ogura et al., 2006) or Lola (Buschmann et al., 2009) have MPCF attached to a passively constrained and/or actuated ankle joint in order to realize a stable stance by spanning a global support polygon. Recently developed humanoid robots are equipped mostly with an active ankle joint. The hydraulically-actuated humanoid robot Atlas (Fallon et al., 2014) has 6DoF in each leg and an arrays of strain gauges provide 3-axis force-torque sensing in the foot. The DRC-Hubo robot (Luo et al., 2014) has two degrees of freedom in its ankle joint (roll and pitch). Besides the actuation, with an implemented 3-axis F/T sensors on each wrist and ankle, accelerometers and gyros additional sensory data is available for control. The feet are assembled without any toe joints since the robot has sufficient torque to lift itself easily on one leg. The remotely anthropoid robot CHIMP features motorized tracks on the legs end-effector (Stentz et al., 2015). Of course, with a length of 40 cm and a width of 10 cm these tracks provides a broad and stable base to perform different kinds of tasks. A roll-pitch adaption of the end-effector is not included.

Existing multi-legged walking robots featuring MPCF like Titan (Hirose et al., 1997), Roboclimber (Acaccia et al., 2000) or the foot described in (Tokuda et al., 2003) come along with passive adaptation mechanisms in the feet to exploit these benefits. In the beginning, the BISAM robot was equipped with spherical shaped feet until a bigger support area and a higher friction was desired. Thus MPCF have been installed including a 6DoF force/torque sensor (Albiez et al., 2005). The Aramies robot has actuated claws which are used to get sufficient grip in steep inclinations. Each claw is equipped with five pressure sensors and an IR-distance sensor for ground contact detection (Hilljegerdes et al., 2005). While the mentioned MPCF may be sufficient for effective quadrupedal walking, a stable and efficient locomotion in bipedal walking is also desired for the system presented here. In the area of multi-locomotion robots Fukuda and coworkers presented a robot able to perform both locomotion modes (Kajima et al., 2003). Unfortunately, it is unclear, if the robot has any sensors applied in the feet structure.

Since the combination of the two locomotion modes is our focus, new active MPCF suitable for both locomotion modes had to be developed. In contrast to the mentioned MPCF, we aim to allow a high perception

of the surrounding environment. To deal with the challenge that mobile robots have to master environments with constantly increasing complexity, there is an increased need for sensory feedback. This in turn means increased sensing capabilities are needed. In order to prevent additional computational costs to the main pc and to meet communication constraints, sensor pre-processing units were added. Like the sensors, these units have been directly integrated into the structures of the robot, more precisely, into the feet and spine.

The body itself consists of rigid structural components in the majority of biologically inspired walking systems. As a consequence of these rigid connections, the motion of most robotic systems appears static and restricted. In contrast, spines are used in nature as central elements of vertebrates with several purposes like to add degrees of freedom, to absorb shocks, or to store and release energy to increase the efficiency.

Although some of the above mentioned robotic systems possess one passive or active DoF in their body, structural enhancements are necessary in order to achieve a higher mobility and allow alternative motion sequences. By now, different robotic research groups try to introduce the concept of a spine-like structure in mobile robotics to take advantage of the mentioned characteristics. Or (Or, 2013) investigated the positive effect of the spine on the overall current consumption of a humanoid robot in simulation. He claimed that without a ridged body up to 26.5 % less energy was required while walking. In general, there are two different approaches in spine development: using a passive or an active connection between the front and the rear body. An example for a walking and climbing robot equipped with an artificial passive spine is given by Santos (Santos et al., 2008). The active artificial spines can be subdivided even further according to their setup, depending on whether a serial or parallel alignment is used. In literature, a serial alignment can be seen with different numbers of DoF and different orientations. The salamander robots locomotion is based on the motion of an active spine separated into eight equal segments, which are arranged in a way that all have the same orientation (Crespi et al., 2013).

Within the iCub project (Hinojosa et al., 2006), a humanoid robot shaped as a child was designed featuring a 3-DoF differential based mechanism in the spine to increase the range of motion for the upper body. The robot Petman is an anthropomorphic robot developed by Boston Dynamics and can mimic human upper-body motion due to the 3-DoF installed in its back (Nelson et al., 2012). Ott and coworkers developed the robot Justin which has an actuated torso with four moving axes (three are actuated) to allow a pitch motion of the torso (Ott et al., 2006). Tsujita follows a more parallel alignment and describes an active approach in the design of spine-like structures for multi-legged systems (Tsujita and Miki, 2011), whereby the robots trunk motion is changeable by adapting the elasticity of the pneumatic actuators. Mizuuchi introduced the man-sized humanoid robot Kenta - and later on the robot Kotar - with a flexible spine (Mizuuchi et al.,

2002). The robots show their motion capabilities while sitting but according to Or “no experimental data are available to show that it can stand up”(Or, 2013). A similar tendon-based approach is used by Holland and Knight in their developments (Holland and Knight, 2006).

In this paper we present a legged walking robot with an actuated spine-like structure that is used in locomotion. The artificial spine is a hexapod platform and has, like the MPCF, its own printed circuit boards as well as integrated sensing capabilities. In the following, details relating to the spine design are given and experimental data is shown.

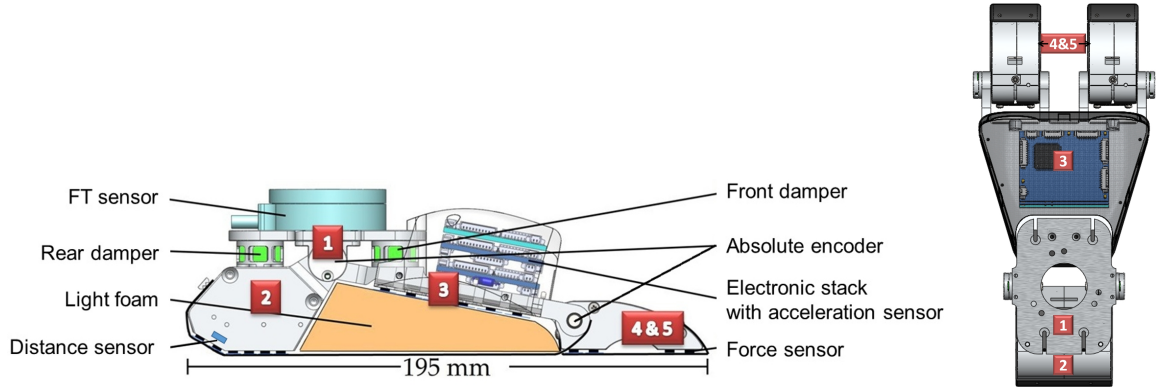
This document is structured as follows: The mechanical design of the proposed robotic system including its subsystems and the required constraints are described in Section 2. The entire design has led to an increased set of sensors, perceiving the system’s state and its interaction with the environment. This results in the need of local sensor preprocessing and local control, as presented in Section 3. In this section an overview of the currently implemented control strategy is given. Sec. 4 begins with a listing of performed experiments and describes the evaluation criteria. In the following, a selected subset of performed experiments for quadrupedal locomotion is described in detail. Besides positive results the issues observed during the field tests are presented, followed by bipedal experiments shown in Sec. 5. This chapter summarizes the capabilities regarding locomotion and mobility of the presented robotic system. Finally, a discussion of the obtained results and an outlook regarding possible future work is given.

2 Mechatronic System Design

The following chapter presents Charlies mechatronic system design. At first, the leg and spine design is presented, followed by a description of the control hardware. Furthermore, a detailed system specification is given. This chapter closes with a description of the communication between the single subsystems.

2.1 Leg Design

The developed MPCF consists of five rigid bodies (see Fig. 2(a)), whereas the connection angles are monitored by absolute angular encoders. Just like its biological counterpart, the rigid core of the artificial foot is supported by multiple layers of different materials for added damping and traction. The foot has the dimensions of 195 mm x 94 mm x 80 mm and a total weight of 350 g including electronics. In (Fondahl et al., 2012) a more detailed description of the design and structure is given.



(a) Sketch of the different foot parts including sensors, electronics, and rigid bodies: leg base (1), (b) Top view image heel (2), forefoot (3) and the toes (4 & 5). Between base and heel as well as between heel and of the foot forefoot a passive DoF is implemented.

Figure 2: The rear multi-point-contact foot as CAD model

As shown in Fig. 2(a), the foot embodies three printed circuit boards (PCBs), two of which are sensor processing electronics with a STM32 microcontroller. Their analog frontend is composed of two multiplexers, an amplifier and an analog-to-digital converter (ADC) to measure up to 49 voltage differences. In the following, this PCB will be referred to as multiplexed data acquisition (MDAQ) board. The third electronics is a connection board which is used to handle the complex cabling of the foot sensors. Additionally, it hosts a 3-axis accelerometer, which allows to measure gravity and other accelerations such as those occurring during collision or slip. The size of the MPCF also makes it possible to equip the foot with other sensors. An optical distance sensor is mounted in the heel, offering the opportunity to reduce the velocity prior to an (un-)expected ground contact. A temperature sensor allows to measure the operating temperature of the MDAQ board as well as a assessment of the functionality of the PCB. The spatial distribution of forces acting on the sole of the foot is measured by a pressure-sensing array consisting of up to 49 force-sensing resistors. With this array, a spatial resolution of 0.3 mm^2 to 4.5 mm^2 and a sensitivity of $20 \frac{\text{mN}}{\text{cm}^2}$ can be achieved. The differences in the spatial resolution is due to the amount of sensors in the respective structures. 15 sensors are implemented in the heel, two times eight in the toes, twelve in the foot arch and 6 around the foot to determine the position of an undesired contact with the environment. Heel and toes have a higher sensor density, because the main load while walking is applied here. The geometric dispatching of the array is presented in (Kuehn et al., 2014). To be able to measure total forces and torques with high accuracy, on top of each front and rear foot an ATI nano 45 6-DoF force/torque sensor is mounted. This sensor is also used as a mechanical interface to connect all feet to the lower thighs, allowing the system to perceive its complete ground interaction forces.

In contrast to the rear feet, the front feet are hook-shaped and equipped with tape switch sensors, which allow

a spatial resolution of about 2 cm of the applied force. A hook-shape was chosen to meet the requirements regarding size and leg proportions, simplicity of form, and functionality. With this design, the front feet do not need an additional active degree of freedom and are generating a line contact to the ground. The spatial distribution of forces acting on the front foot is sufficiently precise for calculating the support polygon.

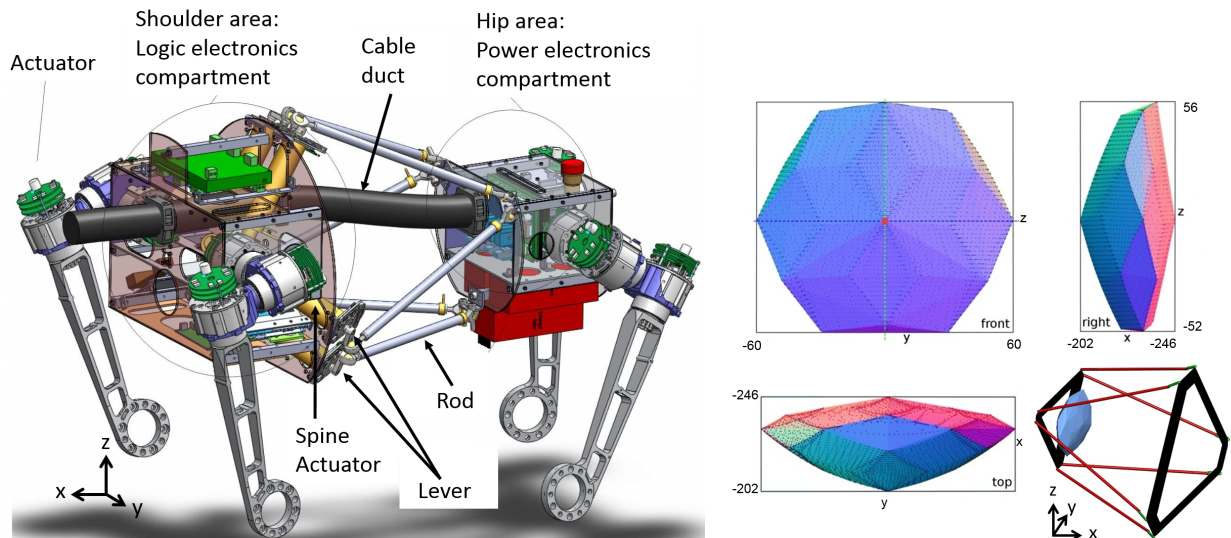
To realize a foot motion, the lower thighs include ankle joints with a double-lever mechanism driven by two brushless direct current (BLDC) motors with 10:1 reduction gears. These motor's drive lead screws and spindle nut mechanisms with 2 mm inclination per turn. This mechanism drives the pitch and roll DoFs of the foot (which are controlled by FPGA-based electronics) whereas the third DoF is kept passive (yaw). To allow the implementation of local control loops, the inverse kinematic is calculated locally in the FPGAs. All three DoFs of the ankle joints are monitored by absolute angular encoders. Above the ankle joint motors, the knee DoF is implemented. Between the three DoFs in the hip and the knee joint a further motor is mounted, moving the toes via cable pull, as it can be seen in Fig. 1(a), in orange on the robots right rear leg. The control PCB for both, knee and toe actuator, is located on the back side of the thigh. A more detailed description of the ankle joint and leg design can be found in (Kuehn et al., 2012).

2.2 Spine Design

The major goal of the artificial spine development was to add extra DoFs to the robot's torso while keeping the design light-weight and robust. The chosen design follows the principle of a Stewart platform. Figure 3(a) shows the spine with its mechanical interfaces for the robot's limbs as well as compartments for the rechargeable battery, control, and power electronics. The spine is driven by six BLDC motors with 246:1 reduction gears. 20 mm levers connect the motors with the 250 mm long rods to realize a hexapod structure using rotational actuators. The diameter of the spine is 305 mm in the front and 190 mm in the rear. The weight of the spine module including motors, levers, rods, casing, and electronics is approx. 3.3 kg.

The resulting workspace of the hip with respect to the shoulder due to the actuated spine is shown in Fig. 3(b). On the left hand side the workspace is shown in y/z coordinates, the hip can move to the left or right (y -axis) and up or down (z -axis). The image on the right shows the side view of the range of motion, whereas the distance between hip and shoulder can also be changed (x -axis). For a more detailed description of the proposed artificial spine design, please see (Kuehn et al., 2013).

Based on the hip workspace, Fig. 4(b) shows the extended range of motion (lateral view) of an attached end effector. The red circle indicates the Range of Motion (RoM) of the leg itself, whereas the green circle takes



(a) Exemplary presentation of the artificial spine. Also displayed are (b) Resulting workspace (in mm) of the hip relative the compartment boxes for electronics in the rear and front, forming the to the shoulder, if the spine is moving robot's torso.

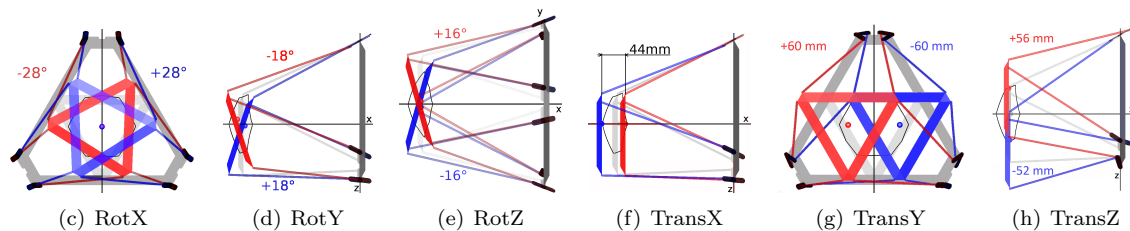


Figure 3: The robots artificial spine (a) and possible range of motion of the hip, if the shoulder is fixed (b). In diagrams (c), (d), and (e) the hip rotations about two axes are locked. In diagram (f), (g), and (h) two translations are locked.

movements of the active spine into account. Depending on the end effector position, its workspace increases between 6% to 16%. In a two-legged pose, for example, objects can be transported from the right side of the body to the left by spine actuation only.

In order to get the spinal subsystem as self-contained as possible, two electronics are used within the spinal structure. The first handles the motor control as well as the calculation of the inverse kinematics. The second is the afore mentioned MDAQ sensor processing board, which calculates the forces and torques between front and rear bodies by means of the current spine pose and six miniature load cells which are integrated into the spine rods. Because only tension and compressive loads can occur within the spine's structure these load cells are sufficient to derive a force and torque vector (Kuehn et al., 2014).

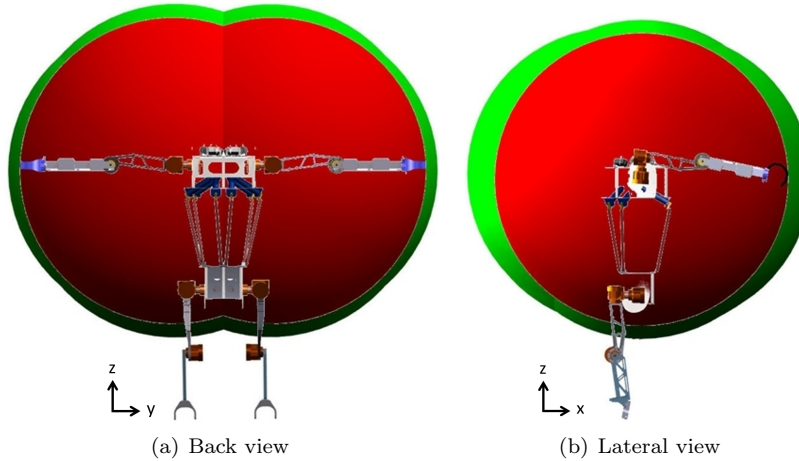


Figure 4: Schematic drawing of the range of motion of Charlie's front limbs with and without spine actuation

2.3 Control Hardware

The body of the robot Charlie was designed to be light-weight, robust, and as small as possible. However, it had to provide enough space for the integration of the electronic systems as well as the cabling. The front body contains the electronic system that deals mainly with the robot control, whereas the rear body is equipped with the power electronics and the batteries.

Figure 5 shows a block diagram overview of the electronics and sensors within the system. The motion control unit (MCU) is the central node that generates the desired joint poses, sends them to the respective joints, and handles incoming motor and sensor data. The MCU has been developed based on an Overo Gumstix board. It features an OMAP3530 using an 720 MHz ARM Cortex A8 core. In addition, it is equipped with 512 MByte NAND-Flash, 512 MByte DDR memory, a microSD card slot, and a WiFi module. This node executes a Linux kernel which handles the multi-threaded control program. The overall robot control is described in more detail within the next section.

In order to use the Gumstix within the robotic system, two additional boards have been developed, to be able to connect the robots peripherals. The main board hosts a Xilinx Spartan6 FPGA, which acts as a bridge between the Gumstix board and some peripheral components such as Ethernet and UARTs. Another task for this FPGA is to provide an interface for the communication with up to eight different extension boards via a custom bus protocol. Currently, only one extension board is necessary for the control of all of Charlie's current capabilities. It provides Low Voltage Differential Signaling (LVDS) interfaces for the communication with all four legs and the spine. Additional RS232 channels, RS485 and GPIOs are used to connect to peripherals such as an Inertia Measurement Unit (IMU), a relay board and the head servos. A

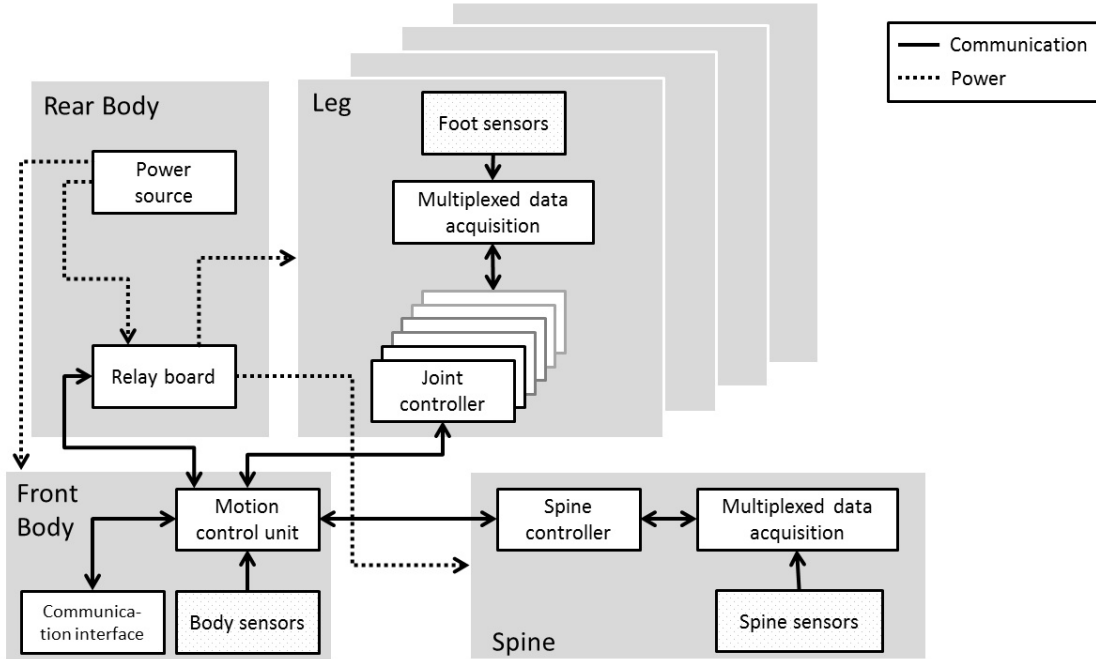


Figure 5: Block diagram of the electronic components and sensors within the system

FPGA was chosen due to the possibility processes data in parallel.

2.4 System Specification

The current prototype has a total of 36 active and six passive DoFs including the head. A schematic drawing can be seen in Fig. 6(a), without the six head DoFs. The key properties of the robot Charlie are summarized in Table 1. Inspired by the limb proportions seen in apes, the front and rear legs of the robot are designed differently, whereby the front limbs are 40 mm longer than the rear ones. In contrast to the single-point-contact front feet, the rear feet are equipped with three additional active DoFs, two to actuate the MPCF and one to drive the toes. The yaw DoF and the adaptive foot arch (shown in Fig. 6(a)) are kept passive to prevent the system from distortion and to increase the adaptively of the sole. However, the thighs (including shoulder and hip) are built identically and each leg consists of four BLDC actuator modules. The ankle joints range of motion is 130° for pitch, 50° for roll and 40° for yaw motions. The maximum angular velocities at 48 V are $160 \frac{\circ}{s}$ for pitch and $190 \frac{\circ}{s}$ for roll motion. The lower thigh have a length of 250 cm and a weight of 1200 g.

The lengths of the body segments of Charlie are proportional to those found in Pan troglodytes (Crompton, 1996). The maximum height in a four-legged posture is 800 mm and about 1360 mm in a bipedal posture,

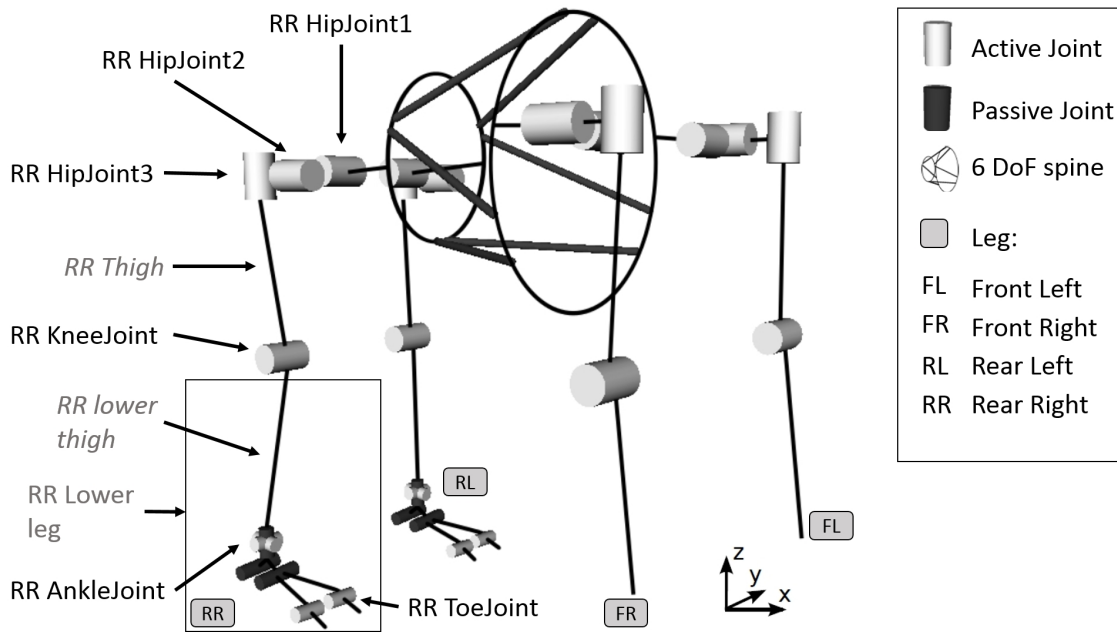


Figure 6: Schematic drawing of the robot's DoFs. The 6 DoF hexapod structure of the active spine is connecting the front and rear part of the body. The red dot indicates the origin of both, reference and body coordinate system (CS) as well as of the world CS at start up.

including the head. The shoulder is 440 mm wide, the hip about 350 mm. Depending on the artificial spine, the distance from the first axis of shoulder to hip joint varies between 500 mm and 544 mm.

Charlie has a weight of 21.5 kg including rechargeable lithium polymer batteries of 44.4 V to 50.2 V with 2.4 A h. The nominal voltage is 44.4 V (twelve cells with 3.7 V each), fully charged each cell has a voltage of 4.2 V, resulting in a voltage of 50.2 V. Charlies battery pack is located in its rear body, close to the power electronics. Front and rear body are each equipped with an inertial measurement unit. For the load free case (no ground interaction forces are applied) the power consumption for the central electronics at 48 V is about 10.5 W, the joint and foot electronics of the front legs need 6 W, due to more sensors and actuators the joint and foot electronics of the rear legs have a power consumption of 9 W, and the spine electronic needs 7 W. The overall consumption is about 47.5 W for the load free case. If the robot is standing on the ground, additional 4.5 W are needed to hold the position. The runtime without external power supply strongly depends on the walking pattern, posture and speed. For the walking pattern presented in the experiment section a runtime of 1 h to 1.5 h is obtained.

2.5 Communication

A robust point-to-point communication system has been developed to interconnect all nodes of the robotic system. At the physical layer, the links operate with low-voltage differential signals via four wires to enable full-duplex data transmission and asynchronous character framing. Above this RS422 like layer, a special high-level data link control protocol (Simpson, 1994) has been established which supports connection-less, light-weight data transmission in asynchronous balanced mode. It also uses the same start-, end- and escape flags but does not include frames other than I-frames, and features a different header format. The resulting frame format of the Node-level Data Link Communication (NDLCom) is depicted in Fig. 7(a).

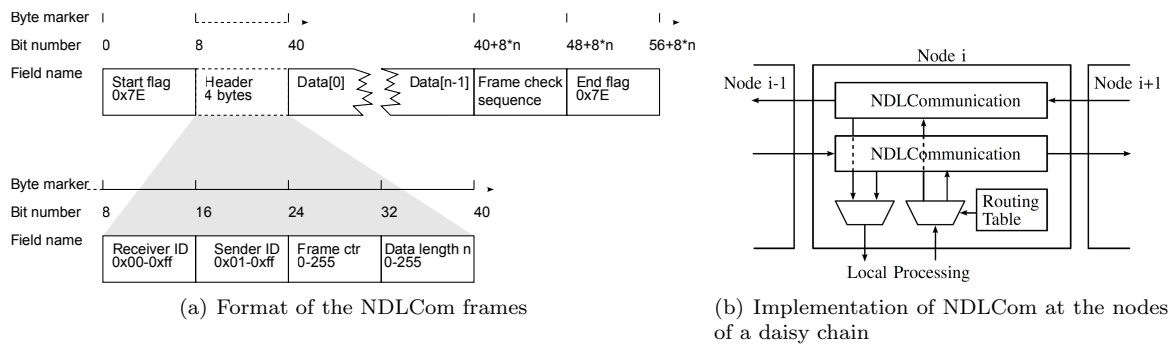


Figure 7: Overview of the Node-level Data Link Communication (NDLCom)

Starting at the corresponding interface of the MCU, the downstream nodes are organized as a daisy chain. A NDLCom instance consists of two inputs and two outputs which are able to receive, transmit, and forward frames. Every node incorporates two of them, one for each direction of the chain. Forwarding is implemented with a cut-through mechanism to reduce latency in comparison to a store and forward technique. Between the link interfaces is a layer responsible for both, routing of outgoing packets from - and sequencing incoming packets to - higher-level processes. Figure 7(b) shows the resulting structure of the interface of a NDLCom node.

Several of such higher-level processes might transmit information dependent on the capabilities of the node. In order to interpret and process, the information type and time of creation are mandatory fields of the layer above NDLCom. The type of data is needed to call different handlers inside a node, whereas the time stamp is needed for link delay compensation or time series analysis. In the following, the actual information like sensor measurements etc. are located. Since all nodes in the system use the same communication mechanism, feed-forward information processing or local control loops can be established in a straightforward and fail-safe manner. Some examples which have been realized are given later in section 3.

Table 1: Key properties of the robot

Dimension (quadruped posture) [LxWxH]	800 mm x 440 mm x 540 mm
Front body dimension (incl. head) [LxWxH]	400 mm x 300 mm x 250 mm
Rear body dimension [LxWxH]	180 mm x 160 mm x 150 mm
Maximum leg length:	
Front	680 mm
Rear	640 mm
Degree of freedom	36 DoF (body: 6, head: 6, front legs: 4, rear legs: 8)
Proprioceptive sensors	34 x motors: position, speed, current, temperature. Feet: acceleration (three axes), temperature, pressure-sensing array (49 elements), 4 x 6 DoF force/torque sensor (one per limb), 8 x absolute encoder (one per toe, one per passive DoF) Spine: 6 x 1 DoF force sensor Body: orientation (three axes), supply voltage
Mass:	
Overall	21.5 kg
Single front leg mass	3.4 kg
Single rear leg mass	4.1 kg
Front body mass (incl. head)	4 kg
Rear body mass	2 kg
Power:	
Power supply	44.4 V to 50.2 V at 2.4 A h (Lithium Polymer)
Power consumption (at 48 V)	
Idle (legs switched off)	10.5 W
Load free (legs switched on)	47.5 W
Standing (in four-walking position)	52 W
Standing (in two-walking position)	50 W
Walking (average in 0°)	65 W
Posture modification:	
Min. / max. body height 2 legged	1060 mm / 1360 mm
Min. / max. body height 4 legged	505 mm / 750 mm
Min. / max. ground clearance 4 legged	225 mm / 470 mm
Min. / max. longitudinal body shift (x-axis) in body coordinates with respect to the initial quadrupedal walking pose	-320 mm / 210 mm
Min. / max. lateral body shift (y-axis) in body coordinates with respect to the initial quadrupedal walking pose	-220 mm / 220 mm
Maximum speed (up to now)	
Forward four-legged	270 $\frac{\text{mm}}{\text{s}}$
Forward two-legged	100 $\frac{\text{mm}}{\text{s}}$
Maximum turning angle per gait cycle (four-legged)	45°

3 Control

This chapter presents the control strategy implemented for the robot. While developing the robot, special focus was placed on a distributed control scheme, in which each subsystem, e.g. joints, spine, and feet features a controller of its own. This way, high parallelization is realized and the calculation costs are divided between several different nodes within the system. The entire system can be seen as a set of nodes, either control, motor or sensor processing nodes and combinations thereof.

Controlling a robotic system with 36 active DoF is a challenging task. The biologically-inspired control approach bases on the control proposed in (Spennenberg and Kirchner, 2007). The concept comprises continuous rhythmic locomotion signals as well as postural activity. To generate an adequate motion, all joints have to be controlled simultaneously in an appropriate manner. The motion control unit has to coordinate and command all subsystems to achieve a synchronized locomotion of the robot. For technical implementation, three parameters (amplitude, frequency, and offset) are used to change the rhythmic movement.

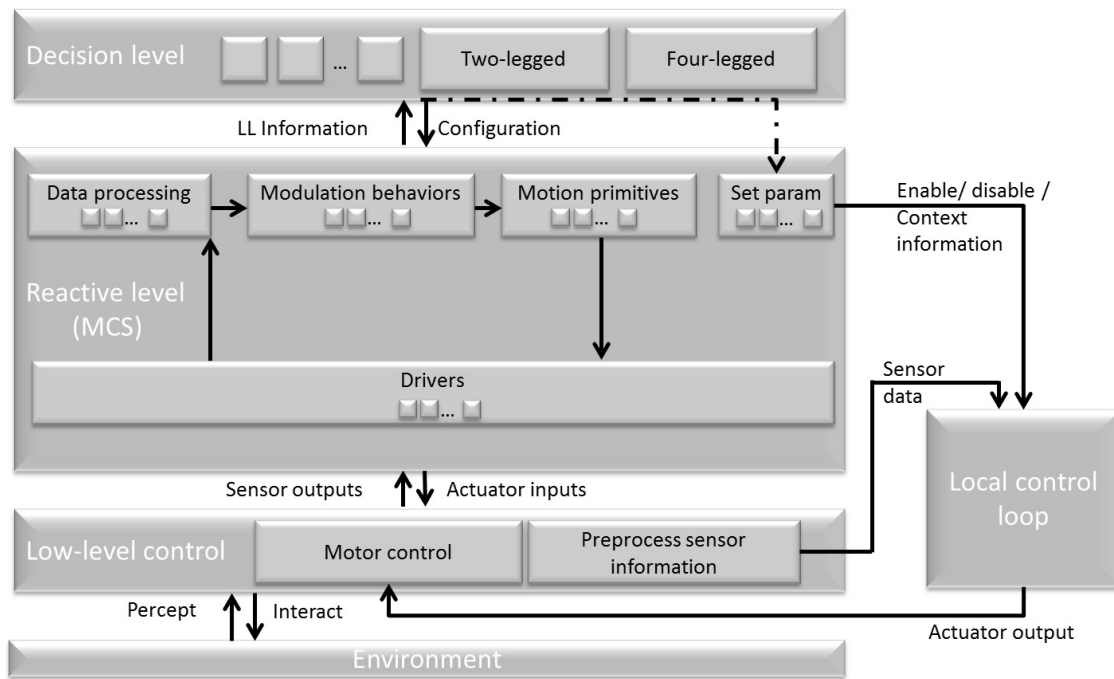


Figure 8: Simplified overview of the robot control. LL stands for low-level.

The robot control software has several layers as illustrated in Fig. 8. While walking, the robot interacts with the environment and gets terrain information by using its sensory disposition. On the lowest level, the sensor data is preprocessed. Due to the distributed control, each joint senses its actual position and is controlled

locally towards the desired position. The local control runs with a much higher frequency of 1 kHz compared to the overall locomotion control of 75 Hz.

3.1 Low-Level Control

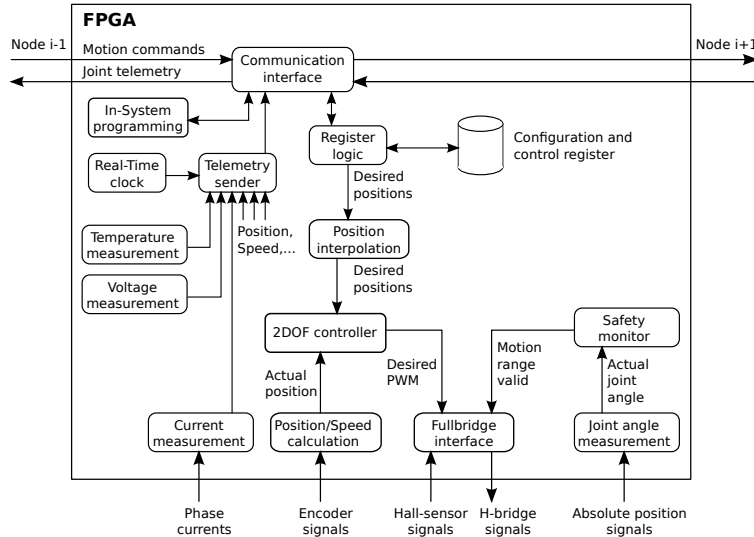


Figure 9: Schematic of the FPGA joint control

In Fig. 9 a joint control scheme is depicted for a single motor joint (e.g. knee joint). In the upper part the communication interface can be seen, which treats all the data packages. The motion and configuration commands are handled by a register logic and most of the configuration values are stored non-volatile in an EEPROM. The desired positions are forwarded to a position interpolation module to achieve smooth control on joint level through position interpolation, which also reduces jitter of the control commands (Ji and Kirchner, 2013). The 2-DoF controller then generates the pulse-width modulation (PWM) outputs for commutation of the brushless motors. A hall-sensor based commutation strategy is utilized to switch the MOSFET's gates of the three-phase fullbridge inverters. The actual position and speed is calculated from the signals of an optical encoder. At startup, the position is initialized by means of an absolute angular sensor. To avoid damage to the hardware, a safety monitor is implemented within the joints where the motors will be turned off if the measured angles by the absolute angular sensors exceed a configured range. Besides position control, a current measurement has been implemented to estimate the load torque of the actuators and will be used by an improved cascaded controller in the future. The measured sensor values are preprocessed locally and sent to the higher level controls.

The FPGA design of the more complex joints (ankle, spine and head) with more than a single motor is a straight forward design. A copy of motor specific control modules exists for each motor. The communication,

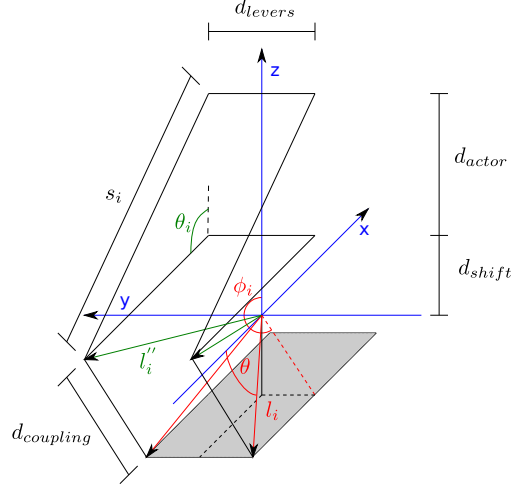


Figure 10: Schematic of the lower leg with respect to foot actuation. All parameters used in theory are shown. Vectors l_i are highlighted in red and l'_i in green (the corresponding angles are also shown).

the register logic, and further modules are handled by an overlaying logic. To achieve as transparent joints as possible, the control commands for these joints comprise desired angles (and translations) from which the desired motor positions are calculated locally by an inverse kinematics module. The inverse geometric model used for implementation in the spine controller can be found in (Takeda et al., 1997).

At first, the origin and orientation of the systems coordinate system has been chosen. The most important point at which all rotational axis meet is the spherical joint. Therefore it is obvious to place the coordinate system at this point. The orientation of the system has been chosen such as to exploit the symmetry of the lower leg. The z-axis coincide with the symmetry axis of the lower leg while the x-Axis coincide with the symmetry axis of the lever pairs. A schematic of the coordinate system including the most important geometric parameters is shown in Fig. 10.

Rotations around two axis through the spherical joint can best be handled by parameterizing the lower lever pair in spherical coordinates (1). The initial angles θ and ϕ_i are fully defined by geometry. θ is the angle of the levers to the negative x-axis and ϕ_i are the angles in the y-z plane.

$$\vec{l}_i = r \begin{pmatrix} -\cos \theta \\ \sin \theta \sin \phi_i \\ \sin \theta \cos \phi_i \end{pmatrix} \quad (1)$$

Then these vectors are rotated around the y-axis (pitch). Afterwards a rotation around the likewise rotated

x-Axis (3) leads to the desired orientation of the lower lever pair with respect to roll and pitch. Equation 2 shows how this is performed. The matrices R are the well-known rotation matrices.

$$\vec{l}'_i = R_{\vec{n}}(roll)R_y(pitch)\vec{l}_i \quad (2)$$

$$\vec{n} = R_y(pitch)\vec{e}_x \quad (3)$$

When the lower lever positions are obtained the higher lever pair are transformed with respect to the coupling constraints. But first the higher lever arms have to be parameterized. Because of the mechanical design the higher lever arms can only rotate in the x-z-plane. This is reflected in choosing cylindrical coordinates (4). θ_i are the angles to the positive z-axis, d_{levers} is the distance of the mounting points of the lever arms and d_{shift} is the distance of these points from the origin of the coordinate system. Another constraint is the coupling between lower and higher lever arms. This interaction is expressed in equation 5. $d_{coupling}$ is the length of the coupling part and $A_i = d_{coupling}^2 - a_i$, B_i and C_i are known constants.

$$\vec{l}''_i = \begin{pmatrix} -r'' \sin \theta_i \\ d_{levers} * 0.5 \\ r'' \cos \theta_i + d_{shift} \end{pmatrix} \quad (4)$$

$$\|\vec{l}''_i - \vec{l}'_i\|^2 = d_{coupling}^2 = a_i + B_i \sin \theta_i + C_i \cos \theta_i \quad (5)$$

$$\xrightarrow{\text{sinusoid}} \theta_i = \arccos \frac{A_i}{\sqrt{B_i^2 + C_i^2}} + \arctan \frac{B_i}{C_i} \quad (6)$$

The obtained angle of the higher lever pair to the positive z-Axis is used to calculate the linear actor extension s_i . The law of cosine leads to the desired extension (7). Here, d_{actor} is the distance of the actor to the higher lever pair mounting.

$$s_i = \sqrt{d_{actor}^2 + r''^2 - 2d_{actor}r'' \cos \theta_i} \quad (7)$$

3.2 Reactive Control in the Motion Control Software (MCS)

The overall robot motion is generated in the reactive level to control the position and orientation of the feet. In the robot control software, the desired joint angles are calculated with high priority, while low priority tasks such as the calculation of the global support polygon are handled by other threads. Interrupt-triggered command handlers in blocking threads handle incoming data from within the robot or another controlling

instance. The resulting desired joint commands are send via the LVDS daisy-chain to the corresponding joints.

Modulation behaviors like posture adaption can have an influence on the resulting walking pattern. These postural behaviors are responsible for keeping the robot statically stable and offer other behaviors the ability to translate or rotate the body.

To calculate the robots center of support polygon, all legs within the stance-phase are taken into account. For the overall support polygon calculation, a maximum of 16 contact points from each rear sensor array as well as two center points for front legs are used. Due to the sensor placement, 16 points are the maximum possible points which can occur to describe the local convex hull. As mentioned before, the foot contains its own sensor processing electronics (see Fig. 2). Due to this local intelligence, not all sensor data coming from the 49 pressure sensing elements has to be used for this convex hull calculation. The foot calculates its own local support polygon and sends only the coordinates of the sensors which represent the edges of the polygon. The expanse and center of the polygon are calculated, followed by a center of pressure calculation, based on the values coming from the force torque sensors. Thereby it makes no difference whether the robot is in its four-legged or two-legged pose or if it is in motion. Even while walking on two legs, due to the MPCF, a support polygon calculation is possible.

3.2.1 Quadrupedal Walking Pattern

In (McGhee and Frank, 1968), different footfall sequences of quadruped animals are analyzed with respect to their stability margin. One of the theoretically possible sequences is found to have the best stability for an idealized walking system. The chosen walking motion is a statically stable gait. On a flat, non-inclined surface the projection of the Center of Mass (CoM) lies at least on the edge of the support polygon, if one leg is lifted. This gait (“crawl”) is the common walking pattern in nature for low-speed locomotion of quadrupeds. The footfall sequence can be seen in Fig. 11.

The walking is implemented as a time-based state machine and different parameters like stride length and height, cycle time, swing and stance time, etc. can be set. The overall gait progress is always between 0 and 1, whereas at 0 the rear right (RR) leg starts its motion. The cycle ends at 1 and a new cycle starts after the touch-down event of the front left (FL) leg. Furthermore, each leg has its own progress counter starting at 0 with the lift-up motion. This allows a later on phase-based aligning of all sensor data coming from different legs. A frequency change while walking (during acceleration or if desired walking parameters

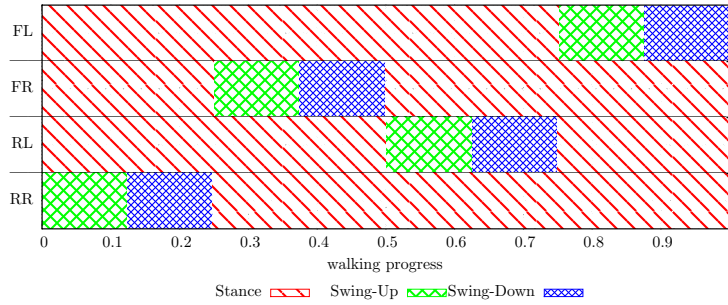


Figure 11: Walking pattern 'Crawl Gait' as used for the following experiments. Beginning with the swing-up of the rear right leg (RR), the other legs are lifted one after another without pauses (FL stands for front left, FR for front right, and RL for rear left).

are changed while walking) does not affect the progress counter.

In general, one step cycle is divided in two phases: the stance, where the foot contacts the ground; and the swing-phase, where the foot moves into the air for limb advancement. The swing-phase includes lift and shift-phase of the foot from the posterior extreme position (PEP) to the anterior extreme position (AEP). The swing-phase and the transitions to and from the stance-phase are implemented by stitching Hermite splines, to obtain smooth leg motions.

The movement of the legs attached to the hip and shoulder can be supported by means of rotations and translations of the actuated artificial spine, so the spine motion alters the trajectory of the feet. A scaling is implemented to define the supported area. By this, the active spine can support only hip, only shoulder, or both. In all cases it is possible to select the influence of the spine to the walking pattern between 0% and 100% online, whereas 0% means no active spine motion at all. In each case (shoulder and hip), the angle and the averaged position between left and right foot are calculated. The desired rotation and translation of the body parts relative to their initial position are then converted into a spinal motion.

To be more specific, if the desired step length is 20 mm per cycle and the spine influence set is to 100% for both, hip and shoulder, a forward motion is realized only through the spine. The spine rotates in a way, that first a leg becomes lifted at PEP and secondly is shifted towards AEP. If, on the other hand, the influence is set to 0%, the hip and knee joints have to drive to cover the set distance.

The range of distance to be covered by the spine is highly specific and depends not only on given rotation and translation offsets (as it can be seen in spine workspace illustration Fig. 3(b)), but also on the footprint. Due to this fact, it is not possible to give a generally valid value about the maximum step length the spine can cover by itself. Figure 3 shows the spines maximum rotations ((c) to (e)). Based on these values, the possible support can be calculated for each pose and footprint.

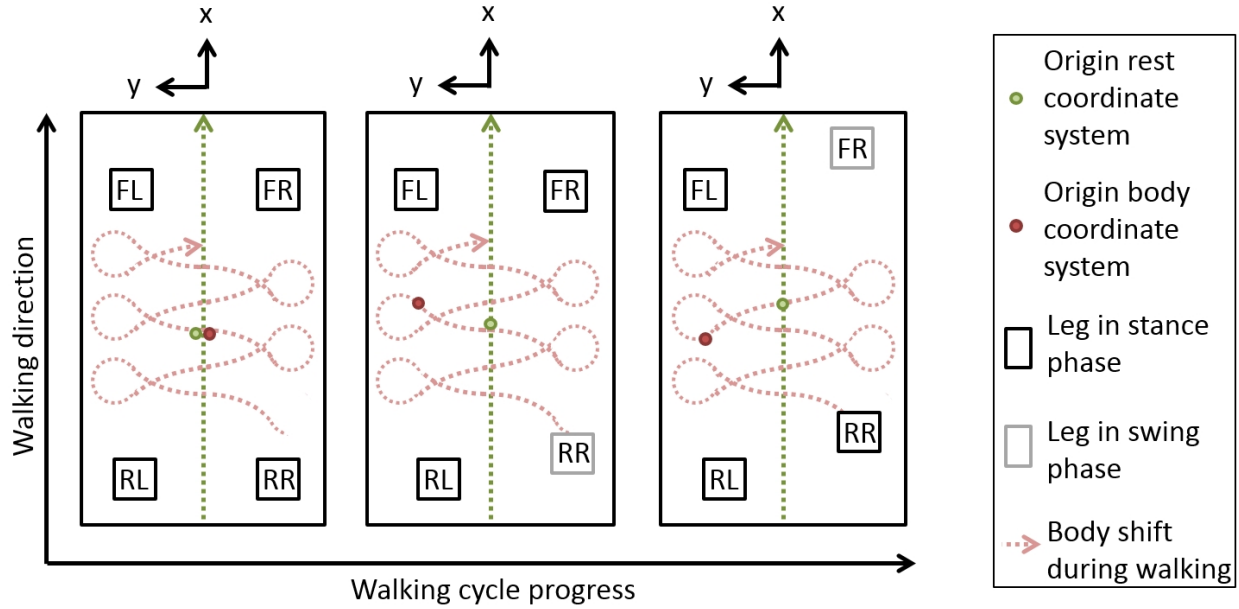


Figure 12: Schematic drawing of the movement of Charlie's *rest*- and *body* coordinate system (CS). The robot stands with all four legs on the ground, thus the origin of both CS is at the same point (left drawing). The right rear foot is in swing-phase, the robot leans itself to the left front leg to shift its CoM (middle). The rear right foot has established ground contact and the front right foot is in swing-phase, thus the body is shifted to the rear left leg (right). The origin of the *rest* CS is not affected by body shifts and rotations.

The trajectory of the feet during a walking cycle can be configured by setting an origin for each leg's motion and an offset for the control point connecting the swing-up and swing-down phase. The length of the stance-phase is derived from the duty cycle and requested walking speed. The duty cycle defines the fraction of a walking cycle, in which a leg is in the stance-phase.

3.2.2 Coordinate Systems

The Charlie robot has a multitude of rotary joints, which enable different subsystems of the system to move independently in six DoF. These subsystems are the four limbs as well as the two body compartments hip and shoulder, connected by the active spine. The head can be moved as well, but is not actuated during walking. The position and orientation of the central body, defined by the axis along hip and shoulder, relative to the *rest* frame is used as an additional virtual limb to influence the center of mass. The central body defines its movement relative to the virtual *rest* system, which is moving along the intended walking trajectory defined by the commands transmitted by the operator. The rotation of the *rest* system is defined relative to the world reference, as it is measured by the IMUs. The actual translation of the *rest* system relative to the world is not known.

If a legs next phase is swing-up (middle in Fig. 12), the goal position of the CoM trajectory is changed to the point diagonal to this leg. This CoM shifting results in an eight-shaped curve for walking on the spot. While walking forward, the eight-shaped curve becomes adapted as indicated by the dashed light red line in Fig. 12. It can be seen that in contrast to the *body* system, the *rest* system is not affected by body shifts and rotations.

The desired translation and orientation of the subsystems are described by a pair of three dimensional vector and quaternions. The usage of quaternions prevents a gimbal lock, for example when the central body is close to an upright position. Since different software modules can influence the same subsystem, their outputs are merged. Three dimensional vectors are summed while quaternions are combined by multiplication.

All limbs, the hip/shoulder and the central body can be influenced by static offsets at runtime, as operator input or from the control system itself. The walking behavior generates output trajectories for the six physical subsystems relative to the rest-position of the robot. The reactive stability controller in turn applies a second layer of movement by changing the virtual subsystem of the central body relative to the rest-system. Finally, the inverse kinematics needs the feet2body and hip2shoulder transformations to calculate the desired joint-angles. Unreachable configurations are ignored by the inverse kinematics and the last valid solution is taken into account.

Two IMUs are mounted on the robot, one to the hip and one to the shoulder, respectively. The known hip and shoulder transformations are used to correct sensor-readings of the IMUs and provide acceleration and orientation data.

3.2.3 Robot Stability

For robot stability, the concept of the Zero Moment Point (ZMP) has been incorporated into control design. In the following, all positions, velocities and accelerations are vectorial entities whereas the arrow has been omitted most of the time. The reference frame of all vectorial entities is the *rest* frame which coincides with the *body* frame if body shift and rotation are zero.

Based on the current CoM position, the current acceleration and the estimated ground plane the ZMP is derived (as shown in Fig. 13(a)). The described walking pattern defines the desired support polygon whose center trajectory is passed to the stability controller. This controller takes the current ZMP and the desired Center of Support Polygon (CoSP) position and CoSP velocity as inputs to adjust the position of the CoM by shifting the body longitudinal or lateral. The difference of the ZMP and CoSP serves as error

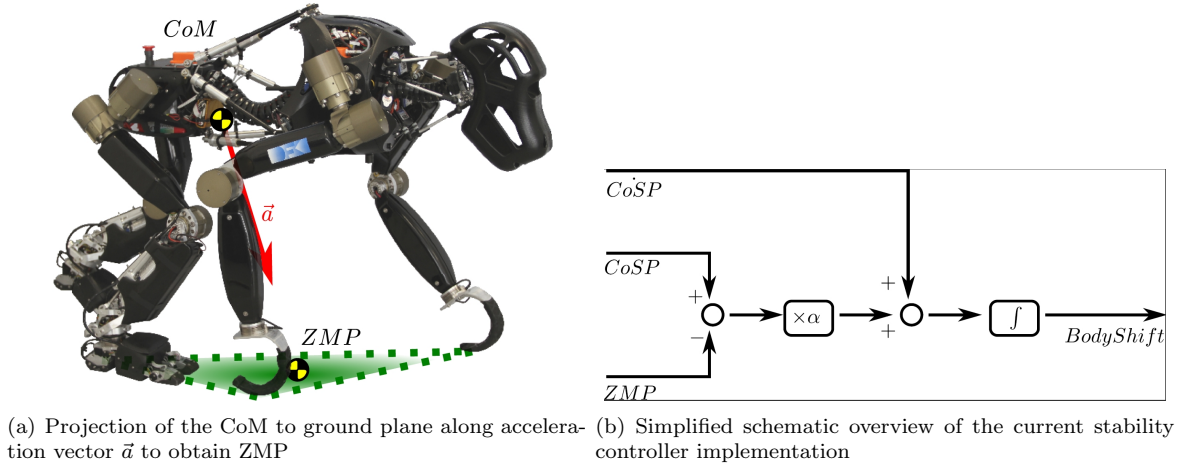


Figure 13: ZMP determination and control

for a proportional-integral controller to compensate disturbances. Velocity feed-forward control improves the tracking accuracy of the desired trajectory such that timing constraints of the walking pattern can be met. Figure 13(b) depicts a simplified overview of the current controller implementation. The implemented controller enables the robotic system to traverse slopes without modifying parameter settings by any operator. Furthermore, the balance controller is independent from the walking and remains active, even if the robot is not walking. All experiments with quadrupedal locomotion were performed using this stability controller.

Later on, the stability controller has been enhanced to allow a better control of bipedal walking. Desired CoSP position, its acceleration $\text{Co}\ddot{\text{S}}\text{P}$ and an estimate of gravitational acceleration \vec{g} are used to obtain a target CoM position at a certain height above ground (inverse pendulum model). A state-space controller with disturbance observer minimizes the error between desired and current CoM position, desired and estimated current CoM velocity as well as the deviation between lastly issued acceleration and current measured acceleration (disturbance observation). In contrast to the previous implementation of stability control, offsets between desired and current CoM due to slopes and disturbances from e.g. shocks are minimized independently. Figure 14 shows an overview of the modified stability controller implementation. This controller has been used for later experiments with bipedal locomotion.

3.2.4 Quadrupedal - Bipedal Posture Transition

Since the aim is to realize an adaptive locomotion transition based on a given context, transition motions are needed to connect the quadrupedal and bipedal walking. One condition to allow a posture change is the termination of the walking process. The transition motion can be seen in Fig. 29 within the experiment

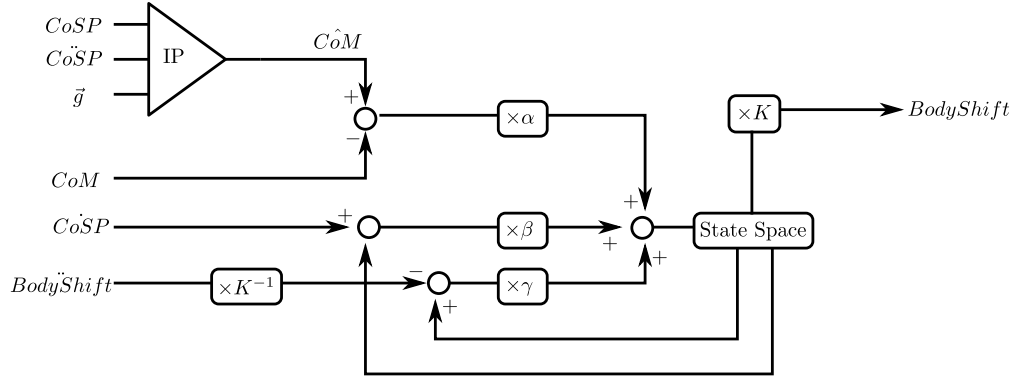


Figure 14: Schematic overview of the modified stability controller. *IP* means Inverse Pendulum model

section (for video material, please have a look on our web page ¹). The motion is divided into different phases. To allow an active balance behavior at all times, the robot has to be controlled in cartesian coordinates. Based on the quadrupedal posture (Fig. 1(a)) in the first phase the robot adapts the rear legs. This is necessary, since we have a narrower footprint when walking bipedal as for quadrupedal walking. In the next step, the center of mass is shifted backwards until it is above the support polygon of the rear legs. In addition to the joints, the spine is actively involved in shifting the CoM. As a result, the front legs soon are load free and no longer needed to support the system. In the final phase, the body is rising to reach its desired position.

The transition from a two-legged posture into a four-legged posture works the other way: the robot bends its knees and rotates the spine, until the front right arm has ground contact. Afterwards, the second arm touches the ground and the CoM is shifted to the center of the support polygon. Once the transition is completed, the respective walking patterns of the robot can be executed. The walking pattern generator does not depend on the specific context in which Charlie is located. The coordinate systems become adapted and parameters like foot swing height or step length are still on the z- or x-axis, respectively. For the experiments shown later on is this particularly relevant.

3.3 Local Control

In general, a distributed system has several components located within some kind of network, where each node has the ability to communicate and thus coordinate its actions. In order to increase the robustness of the systems locomotion in terms of traction and stability a local loop that reacts on the occurring forces and alter the desired trajectories was implemented (a detailed description can be found in (Kuehn et al., 2014)).

¹DFKI Bremen Robotics Innovation Center, <http://robotik.dfki-bremen.de/en/research/projects/istruct.html> July 2015

In contrast to a typical (distributed) control architecture (e.g. shown in (Espenschied et al., 1996)), where sensor data is constantly transmitted to the processing system and the control software uses the information to calculate appropriate counter reactions, e.g. the lower leg structure itself is able to react on the sensory input. By adding these local control loops, a faster response with less bandwidth and less computing power on the primary computer can be realized. Such control loops, in which sensor data is used to alter the desired basic control sequences independently, are currently missing in most robotic systems. Within the Charlie robot this approach has been implemented and local control loops have been established. However, this is not a substitution for global controller, which in general require a certain level of high-level and/or context-based information. Currently, this is not given on the lower levels.

As mentioned before, the system is equipped with one force/torque sensors in each lower leg. Local control loops have been implemented in the rear lower legs, which adapt the ankle angles (pitch and roll) to maximize the area of ground contact of the feet, and thus enhance traction as well as system stability. These loops build virtual springs (VS) which emulate real spring-mass-damper systems by processing measured forces and torques. In contrast to real springs, the spring characteristics (e.g. spring constant and/or moment of inertia) can be adapted at runtime to comply with varying demands. A technical description of this implementation is given in (Kuehn et al., 2014).

In Fig. 15 a schematic illustration of the local control loop within the lower leg is depicted. The ground interaction forces are measured by a force/torque sensor (#1) and processed by a PCB integrated in the feet (#2). As long as the torques do not exceed certain values, an angular offset of the ankle joint is calculated to compensate the torques. This offset request is sent to the ankle joint control electronics (#3), which in turn sets the motors (#4) accordingly to the measured values. Since the motion of the foot has a direct influence on the measured forces and torques, the control loop can be considered as closed. As long as the desired displacement remains within a predefined corridor, the low-level control can adjust it independently from higher level controls. If, however, the desired angular offset is greater than a given epsilon (as deflection of the incoming sensor signal), the low-level has to transfer control to the higher level, where more information of the overall state of the robot is available and the problem can be solved. Since distributed control is a very efficient concept in general (e.g. (Lian et al., 2002)), the control computations can be done locally, allowing a fast method of distributing control over multiple levels, a fast reaction and spatial hardware layouts.

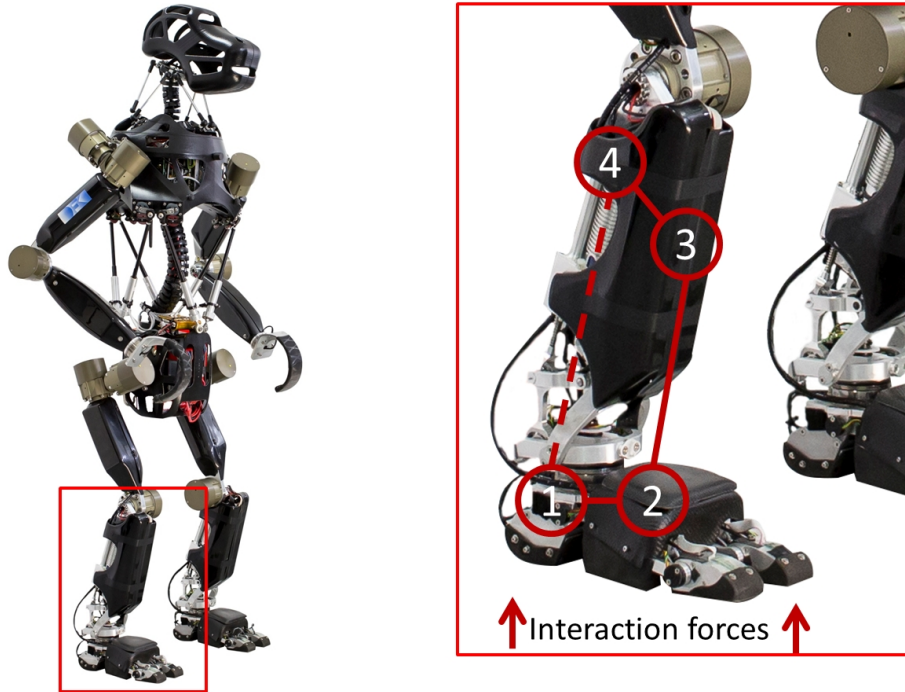


Figure 15: Illustration of the implemented local control loop. The lower limb itself is able to react on the sensory input and produces appropriate counter reactions.

4 Quadrupedal Walking Experiments and Results

The presented hominid robotic system Charlie has a range of capabilities comprising different motion modes, distributed computation, and local control loops. The latter one is a central capability in the context of locomotion. In the following experiment description the authors will show the benefit of the local control loop. Therefore several experiments on different soils and inclinations were performed to verify the current implementation.

The experiments presented in this section and the following chapter however investigate aspects of feasibility and practicality, but also the weaknesses of this software approach as well as on the hardware in general. It can be shown that the use of the local control loop decreases the overall current consumption and increases the robot's stability, allowing the system to overcome unstructured terrain it cannot cover if the local control loop is deactivated. A drawback of the approach is pointed out, as well as an implementation to remedy this deficiency.

For all of the presented experiments, the robot is connected to an external power supply to ensure a constant voltage of 48 V. Please note that the robot was fully equipped at all times, e.g. the batteries are on board,

even though they are not used as power source. Special attention was paid to ensure that the cables does not influence the robot or the experiments at all time. The telemetry data of the robot is transferred via an Ethernet cable; during the recorded experiments Charlie's WiFi capabilities are not used to minimize potential packet loss.

Each plot in this chapter visualizes data from consecutive walking cycles. Each experiment was repeated at least three times and every run produces one single data set. For plotting, the data of one recording is synchronized based on the step cycle progress and unified into a single representative curve, based on the median over all recorded cycles. The minimum and maximum values of the entire recording for one run for this curve are indicated as lightly drawn area in the plot, while the second and fourth quantiles are indicated as more intensely drawn areas.

Information about the state of the walking pattern provided by the control software is used to synchronize data of the legs in two different ways. Either all curves in a plot are synchronized to the same global state of the walking pattern, or the touchdown event of each respective leg is used to phase-align data from different legs. In the latter case, similar events during the cycle of each leg become visible more easily.

4.1 Setups

Figure 16 shows four of five different soils investigated during the experiments. The cycle time of the walking pattern is set to 5 seconds and the feet are lifted 100 mm in swing-phase in all experiments. The system uses a statically stable gait, where it is shifting the projected Center of Gravity (CoG) inside the support polygon created by the feet with future ground contact. One representative walking cycle of the crawl pattern is shown in Fig. 11. It can be seen that all the legs are moving successively, lifting up after each quarter of the total cycle. The movement consists of the swing-up and swing-down phases, whereas ground contact is established during the stance-phase.

The different parameter sets, setups, and terrains are summarized in the following listings. Charlie was tested on *Terrain 1* to *Terrain 4* with each setup, e.g. *Terrain 1* with *Setup 1*, *Setup 2*, *Setup 3*, and *Setup 4*, which results in 16 possible combinations. These 16 combinations were conducted with two different speeds, *Speed setting 1* and *Speed setting 2*, e.g. *Terrain 2* with *Setup 4* and *Speed setting 2*, resulting in 32 different experiments for the quadrupedal motion on ground without incline. Each run was repeated at least 3 times with at least 10 complete walking cycles. A walking cycle is defined as complete after the movement of all four legs (or two legs, for the bipedal case).



(a) Outdoor test track



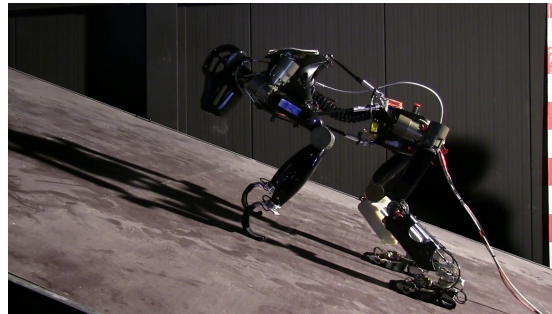
(b) Walking outdoor, *terrain 2*



(c) Walking on grass, *terrain 3*



(d) Walking on gravel, *terrain 4*



(e) Walking up a slope with varying inclinations, *terrain 5*

Figure 16: Experiments with the robot Charlie on different terrain. The outdoor path, grass and gravel field are indicated in a) by the letters according to the sub-figures. The results of the slope experiments presented are gained while walking on an adjustable ramp (e). The sodded outdoor slope contains several different inclinations at a short distance, which is why consistent and reliable data could not be recorded for several steps in a certain incline.

Terrain 5 defines a variable slope with inclinations ranging from -20° to 20° , varied in 5° steps. In inclinations of 20° or more Charlie starts slipping if the parameter set for walking is not adapted. To keep the parameter set for all experiments equal and comparable, with *Speed setting ramp* a walking speed was chosen, where the robot is able to walk up and down without slipping. Again, each run was repeated 3 times with at least 10 complete walking cycles.

- *Terrain 1*: Laboratory, linoleum floor
- *Terrain 2*: Footpath, consisting of sand and pebbles
- *Terrain 3*: Grass
- *Terrain 4*: Gravel, with varying dimensions from 1.5 cm x 1.5 cm x 2.5 cm to 3 cm x 3.5 cm x 4.5 cm
- *Terrain 5*: Variable wooden slope with inclinations ranging from -20° to 20° , varied in 5° steps

- *Setup 1*: Walking without active local control loop and without active spine motion
- *Setup 2*: Walking without active local control loop and with active spine motion
- *Setup 3*: Walking with active local control loop and without active spine motion
- *Setup 4*: Walking with active local control loop and with active spine motion

The term active local control loop refers to the controller implemented in the ankle joint, described in the previous section.

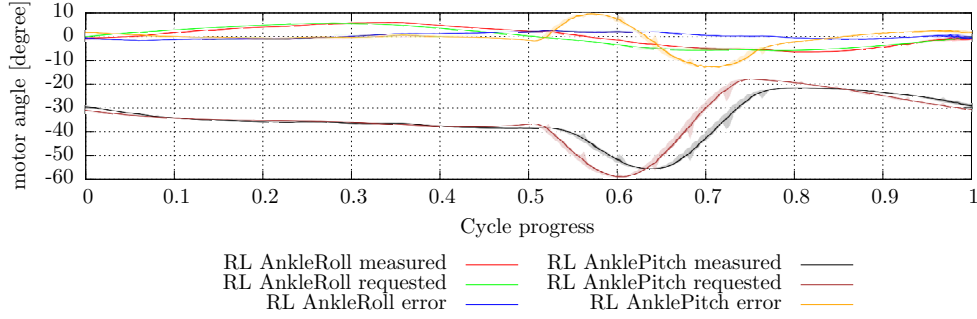
- *Speed setting 1*: Walking with a speed of $60 \frac{\text{mm}}{\text{s}}$
- *Speed setting 2*: Walking with a speed of $90 \frac{\text{mm}}{\text{s}}$
- *Speed setting ramp*: Walking with a speed of $30 \frac{\text{mm}}{\text{s}}$

4.2 Influence of the Local Control Loop

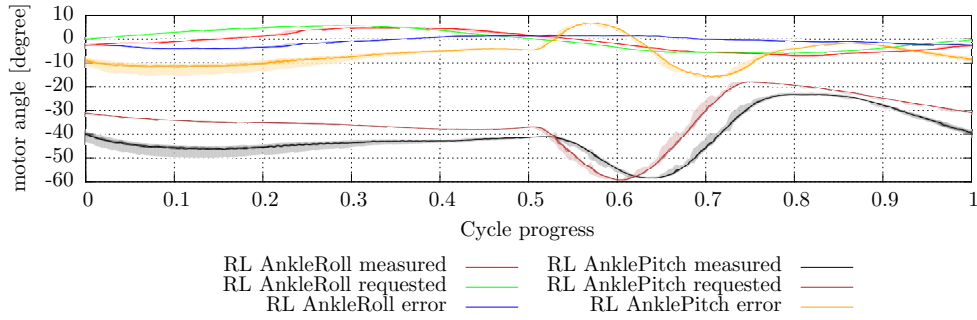
The difference between desired and actual angle of the ankle joint of the rear left leg is shown in Fig. 17 for different setups. In *setup 1*, the desired angle for roll and pitch hardly differs from the reached angle (see Fig. 17(a)). If, however, the local control loop is active (seen in Fig. 17(b)), as desired a deviation over the entire step cycle is recognizable. Since the local control loop only applies limited offset to the given angle, the desired curve is still met between 50% and 80% of the cycle progress in the plot. Therefore, the difference shown in orange and blue (the deviation of the actual from the desired value) between 0% and 50% as well as between 80% and 100% is greater than in the plot without active local control loop.

Figure 18 shows the Zero Moment Point (ZMP) while walking on flat ground with and without active local control loop. The line in this diagrams shows the average ZMP-shifting in x- and y-direction while walking forward. The color indicates the walking cycle progress by changing from green (start of the walking cycle) to blue (end of the walking cycle). The gray bars point out the deviation from the mean value.

As a result of this experiment, it can be observed, that the local control loop has a positive effect on the ZMP behaviour. During walking the ZMP moves much more smoothly, since the ankle joints adapt the feet to the ground. This can be seen in the beginning of the walking cycle between 0.1 and 0.2 as well as between 0.6 and 0.7. By employing the torque-control in the rear legs, the impulse generated by the foot-swing is kept balanced. The swing-phase of the rear leg is between 0.0 to 0.25 and 0.5 to 0.75 of the walking cycle.



(a) Laboratory speed setting 1 setup 1



(b) Laboratory speed setting 1 setup 3

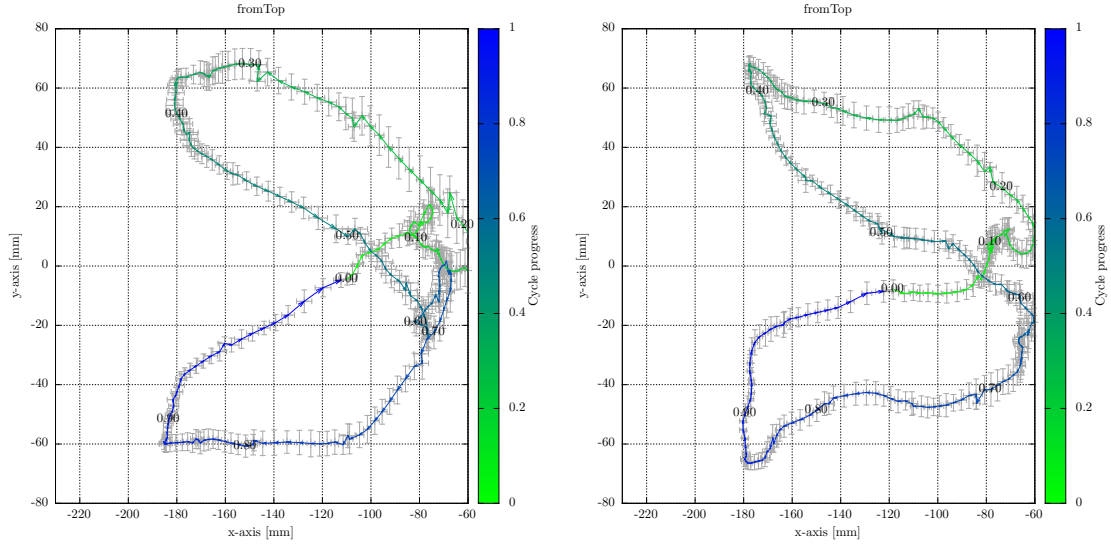
Figure 17: Measured angles in the AnkleJoint in *setup 1* (without local control) and *setup 3* (with local control)

4.3 Impact of Different Terrain on System State

In this section the effects of different terrain substrates on various proprioceptive measurements are investigated. These measurements include the current consumption of the joints and the forces and torques present at the end-effectors as well as in the spine. Additionally, the influence of different walking parameters and behaviors on them are analyzed as well.

4.3.1 Power Consumption

The current consumption of each motor is recorded by each joint control electronics and sent to the Motion Control System (see chapter 3). The load free power consumption of 47.5 W (see Table 1) of the individual electronic systems is not included in the total system current consumption shown in the following plots. Only the current additionally required for the movement is shown. When walking without any additional behaviors, it can be seen that the system needs the most power while moving the body from the left support phase to the right support phase (see Fig. 19(a)). These are the regions 0 to 0.1 and 0.5 to 0.6 relative to the progress of the cycle time. This is mainly caused by the spine, which has to carry the robots weight while



(a) *Terrain 1*: Laboratory floor with *speed setting 1* and *setup 1* (without local control) and (b) *Terrain 1*: Laboratory floor with *speed setting 1* and *setup 3* (with local control)

Figure 18: Walking on flat terrain with and without local control, e.g. torque control in the rear feet. It can be observed that with an active local control loop smaller deviations of the ZMP occur as well as the ZMP follows a more smooth path.

one of the two rear legs performs the swing-phase. The difference is due to a significantly higher weight of the rear legs compared to the weight of the front legs.

In the data shown in Fig. 19, the robot constantly performs a motion sequence with an active local control loop. Except of the local control loop and an active balance behavior, the robot does not react to any unevenness of the ground, e.g. by changing its leg lengths. Individual legs have to bear an increased share of the weight of the robot during stance-phase, if they step on a small obstacle. This is also reflected in a significantly greater min/max-difference and quantile surfaces of the bottom plots, suggesting a less deterministic soil interaction.

If the local control loop is enabled, the current consumption inside the motors is increased in the front left leg (cycle time of 0.4 to 0.6) while the rear right leg executes its swing motion (not displayed). Through the now compliant roll and pitch angle in both ankle joints the weight of the robot is more distributed. As a result, the robot legs are less tensed up with each other, therefore the overall current consumption decreases, as it can be seen in Table 2. This behavior can also be observed at higher speed, as shown in the second line.

While walking on uneven terrain (see Fig. 19(d) and Fig. 20), the motor current increases slightly by about 100 mA to 200 mA, as it can be seen in the first two plots in comparison to the second two plots of Fig. 19. The

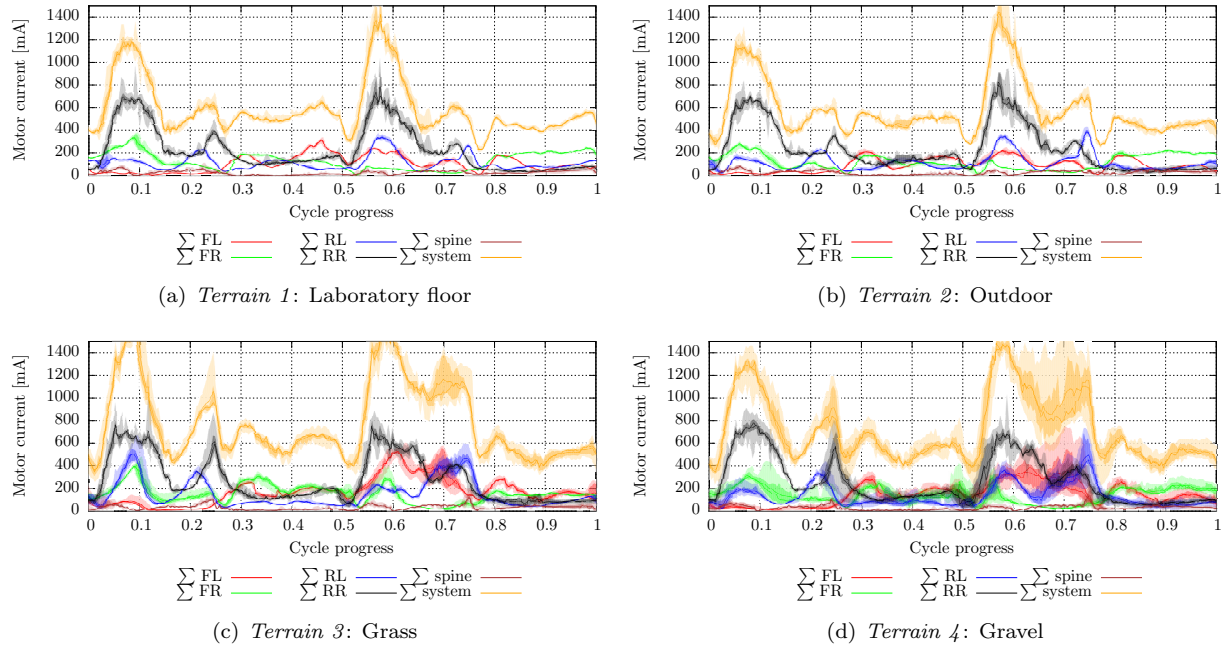


Figure 19: Sum of the motor currents of all subsystems while walking on different terrain. The data shown is from experiments with *setup 3* with *speed setting 1*.

Table 2: Power consumption while walking on *terrain 1* (mean values of one complete step cycle)

Configuration/ Walking speed	<i>Setup 1</i> in [W]	<i>Setup 2</i> in [W]	<i>Setup 3</i> in [W]	<i>Setup 4</i> in [W]
<i>Speed setting 1</i>	35.5 (± 1.5)	35.5 (± 1.5)	31.7 (± 1.0)	32.1 (± 1.5)
<i>Speed setting 2</i>	52.8 (± 2.0)	55.2 (± 2.0)	47.5 (± 1.5)	49.5 (± 2)

reason is the inactive ground-adaption behavior of the robot. Table 3 shows the average power consumption for the same setup and parameter sets like before but walking a different ground. It can be seen that the power consumption is higher compared to walking on *terrain 1* shown in Table 2 and also the standard deviation increases. Due to the uneven ground, no step is like the previous step. This effect is even more clearly visible when the robot moves faster on the gravel field, as shown in the Table for *speed setting 2*.

Table 3: Power consumption while walking on *terrain 4*: Gravel (mean values of one complete step cycle)

Configuration/ Walking speed	<i>Setup 1</i> in [W]	<i>Setup 2</i> in [W]	<i>Setup 3</i> in [W]	<i>Setup 4</i> in [W]
<i>Speed setting 1</i>	40.0 (± 6.2)	41.2 (± 7.5)	40.0 (± 6.2)	44.0 (± 8.5)
<i>Speed setting 2</i>	n.a.	n.a.	77.0 (± 36.0)	60.0 (± 12.0)

More interesting than the slightly reduced power consumption is the fact that the robot is not able to overcome the gravel field when the local control loop is not active. Thus no reliable data could be recorded for the experiment for *setup 1* and *setup 2*. However, in the setups with active local control loop the robot was

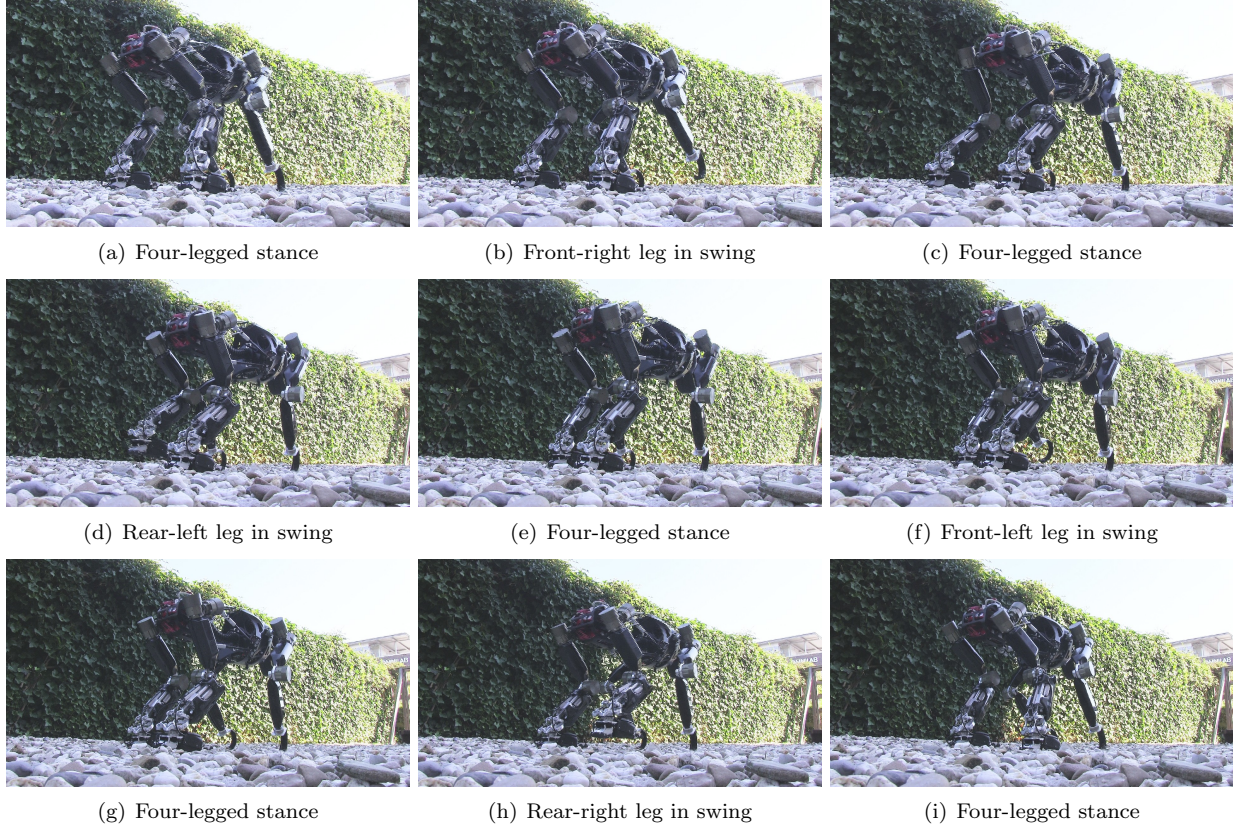


Figure 20: Walking in a gravel field

able to cover the field, even though the current consumption and standard deviation increases significantly. This indicates how useful an additional local control level for Charlie can be, even if it is detached from the main controller supervision.

In summary, it can be said that besides the observation that with an active local control loop in general smaller deviations of the ZMP occur as well as the ZMP follows a more smooth path, the local control loop makes it possible in the Charlie robot to reduce the energy consumption. Furthermore, it enables the robot to deal with unstructured environments, which it could not pass through in a stable manner, as the local control was turned off.

4.3.2 Forces at Feet

In this section, the results of the foot force measurements are presented. First, the results for walking on *terrain 1*: Laboratory floor with *speed setting 1* for all different setups are shown in detail. In the following, the data from walking with *setup 1* and *speed setting 1* on the various substrates is discussed. The ground interaction forces while walking can be measured by the four force/torque sensors. They are influenced by

the walking pattern, soil characteristics, active spine motion, and the local control loop. In Fig. 21 and Fig. 22 the applied forces of the left front and left rear leg are represented.

In Fig. 21, the influence of the phase changes can be recognized. At 6% of the walking cycle, the momentum introduced by the lift-up movement of the rear right leg briefly causes a measurable force reduction at the front left leg. After decay of this dynamic effect, the force rises up again in z-direction. At 50%, a second minimal decrease occurs due to similar effects resulting from the CoM shifting from the robots right hand side to its left hand side. A reduction in force can be seen in each of the four plots, but is more distinct with active local control loop. This can be explained by the adaption of the rear feet to tensing momenta. In the walking cycle the front left leg is in swing-phase at 78%. Therefore forces tend to zero.

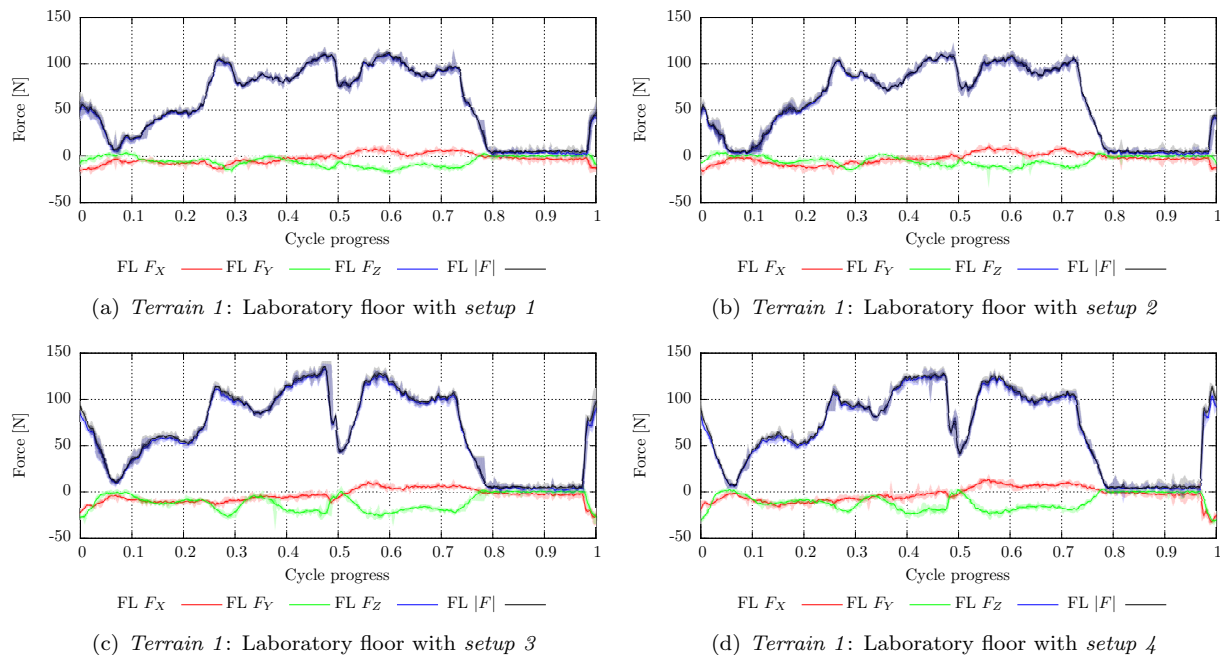


Figure 21: Measured forces of the front left leg in different setups with *speed setting 1*

In Fig. 22 force measurements of the rear left leg are shown. Between 54% to 73%, this leg is in its swing-phase. By comparing data shown in Fig. 22(a) with the one in Fig. 22(b), one can see that the initial peak forces (between 0% and 10%) are reduced as soon as the local control loop is active. In addition, at the end of one step cycle it can be seen that the average measured force is smaller as well. Comparing Fig. 21(a) with Fig. 21(c), and Fig. 21(b) with Fig. 21(d) respectively, one can see that with active local control a higher maximum force in z direction is acting on the FL leg. But at the same time, the local control reduces the acting forces at about 50% of the cycle progress so that overall they cancel each other out. The measurements of the front and rear right leg are comparable to the one shown in Fig. 21 and

Fig. 22. Therefore they are omitted.

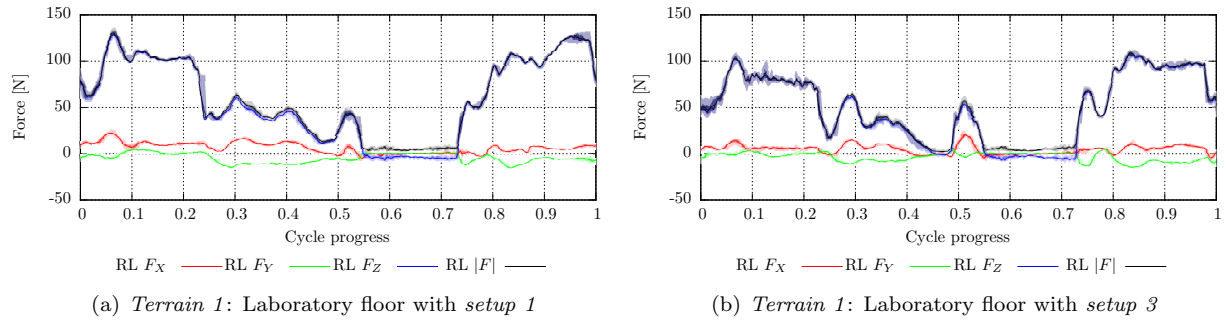


Figure 22: Measured forces of the rear left leg in different setups

4.3.3 Force at Spine

Table 4 lists forces acting on the spine while walking. The rows and columns show the tested setups and the force in N for x, y, and z axis, respectively.

The data show a reduction of forces along the z-axis of about 60% while walking with an active local control loop. Furthermore, while walking with a faster pattern presented in the lower part of table 4, a mean reduction of about 80% was measured. A significant change in x and y is, however, not observed. In the table, the normalized force can be seen, which is also minimized when the local control loop is active. With increased speed (shown in the example of *speed setting 2*), this effect can be illustrated further. The introduced local control loop not only reduces the forces acting on the feet (see Fig. 22 and (Kuehn et al., 2014)), but also affects the forces acting on the entire robot body.

Table 4: Measured spine force values (mean values of one complete step cycle)

<i>Speed setting 1</i> Setup	X [N]	Y [N]	Z [N]
<i>Setup 1</i>	3.7 (\pm 2.8)	7.7 (\pm 2.9)	-28.6 (\pm 3.1)
<i>Setup 2</i>	2.9 (\pm 2.7)	8.1 (\pm 2.7)	-29.3 (\pm 3.0)
<i>Setup 3</i>	5.7 (\pm 2.6)	9.0 (\pm 2.8)	-11.3 (\pm 2.6)
<i>Setup 4</i>	6.1 (\pm 2.9)	7.6 (\pm 3.1)	-10.0 (\pm 3.1)
<i>Speed setting 2</i>			
<i>Setup 1</i>	4.3 (\pm 3.2)	7.5 (\pm 3.3)	-26.5 (\pm 3.3)
<i>Setup 2</i>	6.4 (\pm 3.0)	9.4 (\pm 3.1)	-24.6 (\pm 2.9)
<i>Setup 3</i>	7.2 (\pm 3.2)	9.2 (\pm 3.2)	-6.8 (\pm 2.9)
<i>Setup 4</i>	6.6 (\pm 3.2)	8.6 (\pm 3.4)	-5.1 (\pm 2.8)

4.3.4 Torques at Feet

In this section the measured torques of the left front and rear leg are shown. As shown in Fig. 21, the pattern of the curves of *setup 1* and *setup 2* as well as of *setup 3* and *setup 4* are nearly identical, therefore Fig. 23 will show data of *setup 2* and *setup 4*.

The measured torques at the front legs are significantly smaller compared to the ones in the rear legs (Fig. 23). This is to be expected, since the ground contact area on the front legs is significantly smaller than the one on the rear legs. Since the force/torque sensor is not the ground contact point, some of the ground contact point forces have an effect on this sensor as torque. When the front left leg is raised (at 0.75 of the cycle progress), the measured torque values drop to zero since there is no ground contact. In comparison to experiments performed with and without spine motion, no differences in the measured torque in the foreleg can be seen. If the local control loop is enabled, a change in the values of the torque measured can be recognized: the maximum torque increases minimally of about 1 N and fluctuations in the measured torque, that come hand in hand in time with the raising or lowering of the feet, are slightly stronger.

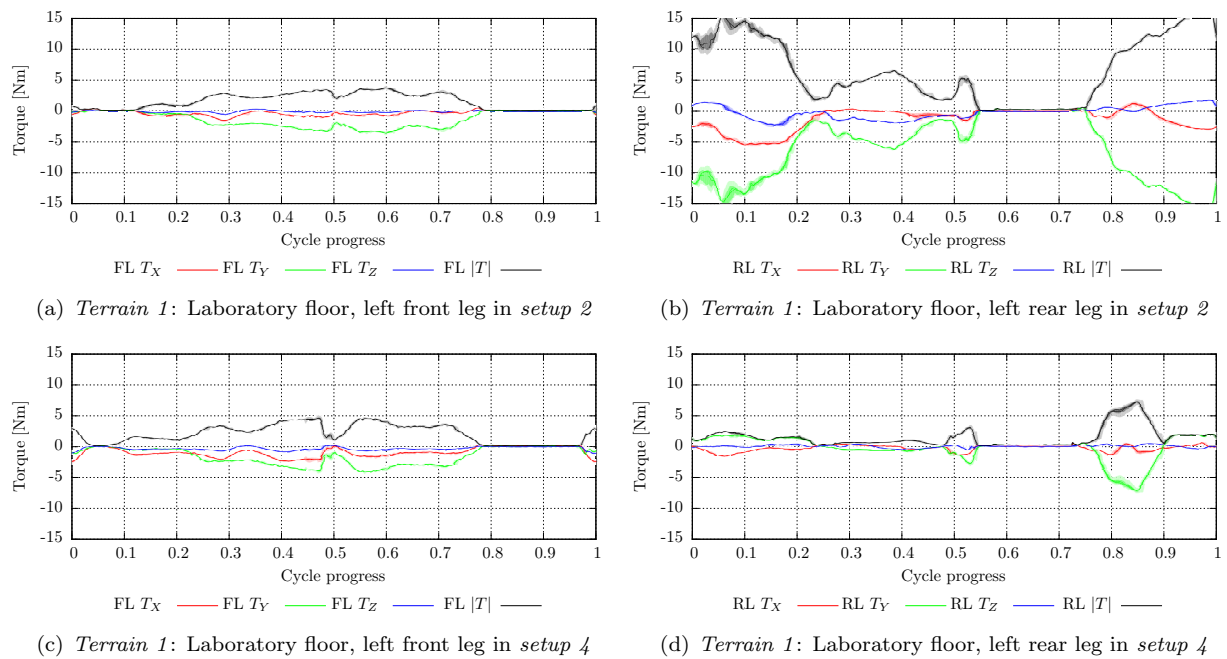


Figure 23: Measured torque of the front and rear left leg in *setup 2* and *setup 4*

The torques occurring at the rear legs (shown in Fig. 23) are considerably stronger than the torques measured in the front legs (if the local control loop is not active). In contrast to the front legs, it is noticeable that at the beginning of swing-phase of the rear left leg (at about 0.5) the torques rise briefly, regardless of whether the local control loop or the motion support through the spine is activated or not. If the local control

loop is activated, the measured torques in the rear legs are much smaller. This is to be expected, since the occurring torques are reduced by the active compliance. A significant difference in the data with and without the movement of the spine can not be determined. With a disabled local control loop, the movement of the spine has only slightly affected the measurements: the torques increases at 0.1 minimally stronger and at 0.35 there is a slightly difference in the graph over time.

4.3.5 Torque at Spine

The applied torque in z-axis behaves similarly as the corresponding force: the moment is nearly reduced to zero with the local control loop. Strikingly, the local control loop also has a strong influence on the acting torque on the x- and y-axis as opposed to the measured forces. In addition, the reversal of the sign is particularly noticeable. Once the local control loop is active, a decreased torque value of the x-axis and a change in the sign can be observed. This also applies for the torques on the y-axis. While walking with *speed setting 2* this becomes even more noticeable. With this parameter set, the x-axis mean value decreases even more, which can be explained by a more dynamic leg movement. As with the forces, the normalized torques applied to the spinal structure is reduced, if local control loop is turned on.

Table 5: Measured spine torque values (mean values of one complete step cycle)

<i>Speed setting 1</i> Setup	X [N]	Y [N]	Z [N]
<i>Setup 1</i>	14.5 (\pm 3.3)	8.8 (\pm 2.7)	-20.9 (\pm 2.9)
<i>Setup 2</i>	16.9 (\pm 3.4)	7.9 (\pm 2.7)	-17.7 (\pm 2.9)
<i>Setup 3</i>	-2.4 (\pm 2.9)	-10.8 (\pm 2.7)	1.6 (\pm 2.7)
<i>Setup 4</i>	-1.8 (\pm 3.4)	-8.1 (\pm 3.3)	1.0 (\pm 3.0)
<i>Speed setting 2</i>			
<i>Setup 1</i>	12.4 (\pm 3.5)	8.3 (\pm 3.5)	-20.4 (\pm 3.4)
<i>Setup 2</i>	9.3 (\pm 3.4)	5.9 (\pm 3.3)	-20.0 (\pm 3.2)
<i>Setup 3</i>	-8.1 (\pm 3.3)	-12.4 (\pm 3.0)	0.7 (\pm 3.0)
<i>Setup 4</i>	-7.0 (\pm 3.2)	-10.3 (\pm 3.1)	1.0 (\pm 3.0)

4.3.6 Conclusion on Flat Ground Experiments

This section summarizes the results obtained on a flat and even surface. All the mentioned results relate to the developed hominid robotic system.

In the beginning it was observed, that the local control loop has a positive effect on the ZMP behaviour, since a lower standard deviation was recorded and thus the optimal and predicted CoM trajectory is met more precise. Besides the positive effect on the ZMP behaviour, the local control loop makes it possible

in the Charlie robot to reduce the energy consumption. Furthermore, it enables the robot to deal with unstructured environments, which it could not pass through in a stable manner, as the local control was turned off. The force measurements show a reduction of occurring forces is more distinct with active local control loop. This can be explained by the adaption of the rear feet to tensing momenta. If the local control loop is activated, the measured torques in the rear legs are much smaller. This is to be expected, since the occurring torques are reduced by the active compliance. As with the forces, the sum of the torques applied to the active spinal structure is reduced, if the local control loop is switched on.

The experimental data show that the implementation of the local control can be useful in this robot. In the further course, the local control loop development will be tested in different inclinations.

4.4 Walking on Various Inclines

The following section describes experiments with the robot walking on different inclinations, whereas *setup 2* and *setup 4* will be presented more in detail than the other two setups, to show the results of the local control. The sodded outdoor slope contains several different inclinations at a short distance. Each step would result in a change of the body pitch, which is why consistent and reliable data could not be recorded for several runs. To produce repeatable results, an experimental setup was chosen where each inclination is kept constant for a longer distance. Nevertheless, the inclination on the ramp is freely adjustable. The slopes were set in 5° steps from -20° to 20°, whereas a positive degree means the robot is walking up-hill and a negative describes down-hill walking. Figure 24 shows Charlie walking in 20°.

Each setting of the ramp has been tested four times covering a distance of at least two meters (therefore at least 14 complete step cycles). *Speed setting ramp* was used, since this set produced a stable locomotion in all eight cases. The robot walks forward with $30 \frac{\text{mm}}{\text{s}}$ at a total cycle time of 5 s. A safety harness, which could distort the results, was not used. The inclination of the system is balanced by active ZMP control. While performing all experiments, no parameter aside from the inclination has been modified.

4.4.1 Influence of the Active Spine

The active spine allows a reduction of maximum needed speed of each individual joint within the legs while walking. In Fig. 25, the maximum joint velocity of the right rear knee is shown while walking in all tested slopes. Although it has been stated in the beginning of this section that only *setup 2* and *setup 4* are considered, it has to be shown that the local control loop has no negative influence to the maximum joint

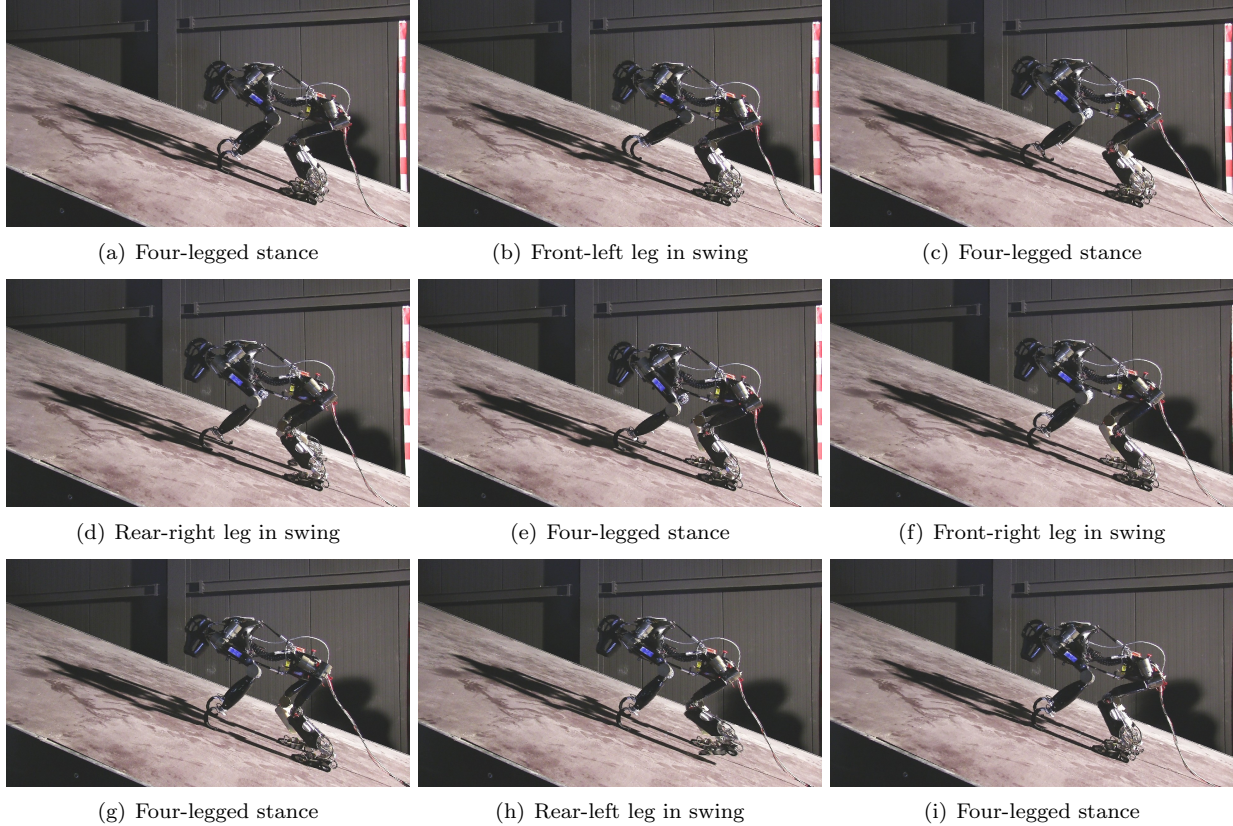


Figure 24: Walking up-hill on a 20° slope

velocity. Therefore, Fig. 25 includes also *setup 1* (red line), which is a setup without spine motion. *Setup 2* (in green) and *setup 4* (in blue) differ only in the activation of the local control loop. It can be seen that the maximum joint velocity is reduced at all times between $10 \frac{\circ}{s}$ and $15 \frac{\circ}{s}$, also a reduction of up to 14%. The robots overall power consumption is nearly equal for *setup 1* compared to *setup 2* and *setup 4*. The legs require less energy, but the savings are now used to actuate the spine.

Reducing the maximum velocity has several advantages. Lower joint accelerations result in the robots hardware to be exposed to less mechanical stress, which, in turn, has a positive influence on reliability and lifetime. In addition, shorter step cycles can be performed allowing an increased walking speed of the robot.

4.4.2 Power Consumption

In the following section, the energy consumption of the system in the two setups with spine motion on different slopes is described. The difference between both setups is the activated or deactivated local controller. The values shown in the plots are based on the measured current inside the motors. The load free power consumption of 47.5 W (see Table 1) of the electronics within the joints is not included in the values.

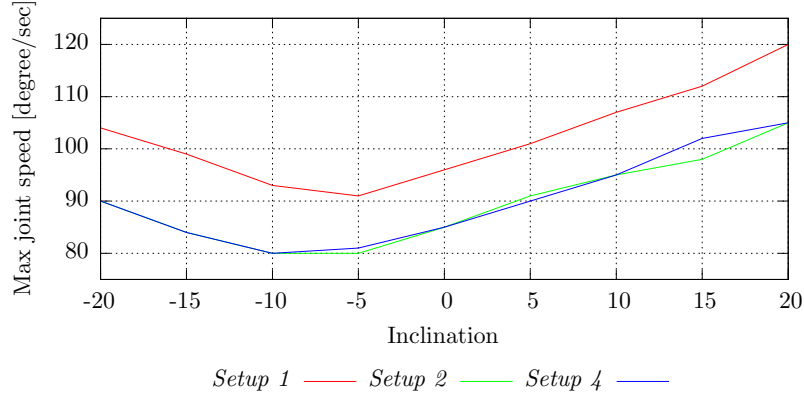


Figure 25: The maximum speed of the RR knee joint per walking cycle at different inclinations

It is expected that the energy consumption increases with an increased inclination. This can be observed in *setup 2*, as shown in Table 6.

Table 6: Using *setup 2* while walking up-hill with different inclinations (rounded to the nearest half)

<i>Setup 2</i>	5°	10°	15°	20°
Run1	35 W(± 2.5)	37 W(± 2.5)	39.5 W(± 3.5)	40.5 W (± 5)
Run2	34.5 W(± 2)	36.5 W(± 2.5)	39.5 W(± 3)	37.5 W(± 3.5)
Run3	35.5 W(± 2)	37.5 W(± 2.5)	41 W (± 3.5)	37.5 W(± 6.2)
Run4	36 W(± 2.5)	37.5 W(± 2.5)	40.5 W(± 5)	37.5 W(± 2.5)
Average Ø	35.5 W(± 2.5)	37 W(± 2.5)	40 W (± 4)	38.5 W (± 4.5)

Table 7: Using *setup 4* while walking up-hill with different inclinations (rounded to the nearest half)

<i>Setup 4</i>	5°	10°	15°	20°
Run1	34.5 W(± 1.5)	34.5 W (± 1.5)	34.5 W(± 2)	34.5 W(± 2)
Run2	35 W(± 2)	34.5 W (± 2)	35.5 W(± 4)	35 W(± 2.5)
Run3	34.5 W(± 2)	34.5 W (± 2)	35 W (± 3.5)	35 W(± 2)
Run4	34.5 W(± 1.5)	34.5 W (± 2)	34.5 W(± 2.5)	35.5 W(± 5)
Average Ø	34.5 W (± 2)	34.5 W (± 2)	35 W (± 3)	35 W (± 3)

It is further observed that the total power consumption of the robot while walking with active spine and local control loop is lower in all positive inclinations compared to walking with active spine only, as it can be seen in Table 7.

Figure 26 displays the measured current consumption of the motors on the ramp with 0° slope (left hand side) for the two different setups *setup 2* and *setup 4*, respectively. Shown are the sums of the motor current for each leg (FL in red, FR in green, RL in blue, and RR in black) as well as for the spine (in brown). In orange, the sum of the legs and spine is displayed to give an impression of the overall current consumption of the robotic system.

It can be seen that the overall average is smaller when the local control loop is active, which is also true for occurring peak values. In Fig. 4.4.2, oscillations of the leg RL and the total current between 0.3 and 0.4 as well as between 0.8 and 0.95 can be seen. The faded colour indicate the minimal and maximal value during all step cycles, while the second and fourth quantiles are indicated as more intensely drawn areas. Thus the faded blue indicate that at least in one step a higher current occurred than in the other steps. If the power consumption in one or more leg has outliers, they also appear in the data plot of the overall power consumption. Less outliers indicate a more repeatable and thus more stable gait. Due to the actuated spine in *setup 2* and *setup 4*, the consumption rises minimally compared to *setup 1* (not displayed).

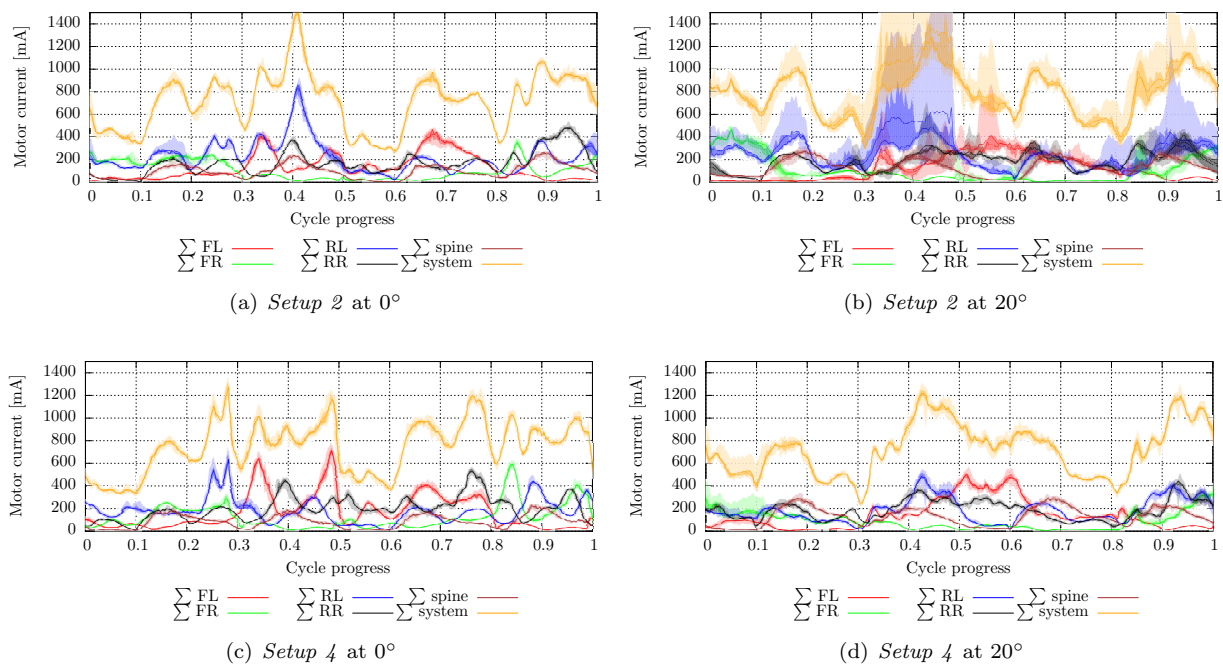


Figure 26: Current consumption of the individual legs, the spine and the entire system in various setups while walking on a slope of 0° and 20°

For comparison, the recorded motor current on the ramp with 20° slope for the two different setups is shown in Fig. 26 on the right hand side. For *setup 4* it can be observed that the current consumption remains unchanged, even if the inclination is increased.

Comparing the power consumption of the front legs in Fig. 4.4.2 to the one in Fig. 4.4.2, one can see that the maximum motor current of the rear legs is decreased with active local control, but the maximum motor current of the front legs is increased. This is due to the different distribution of forces between the legs, as showed earlier. As one might expect, while walking uphill the needed current of the front legs decreases slightly, due to a higher load applied on the rear feet.

A draw back of the local control loop can be seen in down-hill walking. Table 8 shows for *setup 2* the measured power consumption for all runs with negative inclination, Table 9 shows the values for *setup 4*. By comparing the values displayed in Table 8 with the one from Table 9, it can be seen that the overall power consumption increases while walking with active local control loop.

Table 8: Using *setup 2* while walking down-hill with different inclinations (rounded to the nearest half)

Active Spine, no LC	-5°	-10°	-15°	-20°
Run1	35 W \pm 1.5	35.5 W \pm 2.0	37 W \pm 2.5	37.5 W \pm 2.5
Run2	35 W \pm 1.5	35.5 W \pm 2.0	36.5 W \pm 2.5	37.5 W \pm 2.5
Run3	35 W \pm 1.5	35.5 W \pm 2.0	36 W \pm 2.0	38.5 W \pm 2.5
Run4	35 W \pm 1.5	36 W \pm 1.5	36.5 W \pm 2.0	37.5 W \pm 2.0
Average \emptyset	35 W \pm 1.5	35.5 W \pm 2.0	36.5 W \pm 2.5	38 W \pm 2.5

Table 9: Using *setup 4* while walking down-hill with different inclinations (rounded to the nearest half)

Active Spine and LC	-5°	-10°	-15°	-20°
Run1	37.5 W \pm 2.0	42.0 W \pm 2.0	46.5 W \pm 2.5	49.5 W \pm 3.0
Run2	37.5 W \pm 2.0	41.0 W \pm 2.0	47 W \pm 3.0	50 W \pm 3.0
Run3	37.5 W \pm 2.0	42.0 W \pm 2.0	46.5 W \pm 3.0	50 W \pm 3.5
Run4	37.5 W \pm 1.5	42.0 W \pm 2.0	47.5 W \pm 3.5	49.5 W \pm 4.0
Average \emptyset	37.5 W \pm 2.0	42 W \pm 2.0	47 W \pm 3.0	50 W \pm 3.5

In order to ensure comparability, the values of the parameter set were not changed during all experiments. The local control loop parameter set produces a stable walking up- and down-hill, as well as for unstructured terrain, but the statement can be made that this parameter set is not as beneficial for walking down-hill as it is for up-hill walking.

4.4.3 Context-based Adaption

It is sensible to use the local control loop in a context-based manner. The damping constants have to be redefined in order to use them effectively for down-hill walking. As depicted in Fig. 8, the decision level has access to the local control loop and can change its parameter set accordingly to the given context.

Fig. 27 shows the influence of high-level control to the behavior of the local control loop while walking on four legs in different inclinations in an exemplary manner. In contrast to the data in which average values per cycle progress were shown so far, this figure plots the data of one complete experiment over total runtime. Shown are the measured (green) and desired (blue) pitch angle of the right rear leg as well as the robots pitch angle (red), measured by the implemented IMU. The robot was walking up and down a slope with 10° and was performing a turning motion on top of the slope. The turning motion approximately starts at -115 s and is approximately terminated at -40 s. With increased inclines, the local control loop becomes

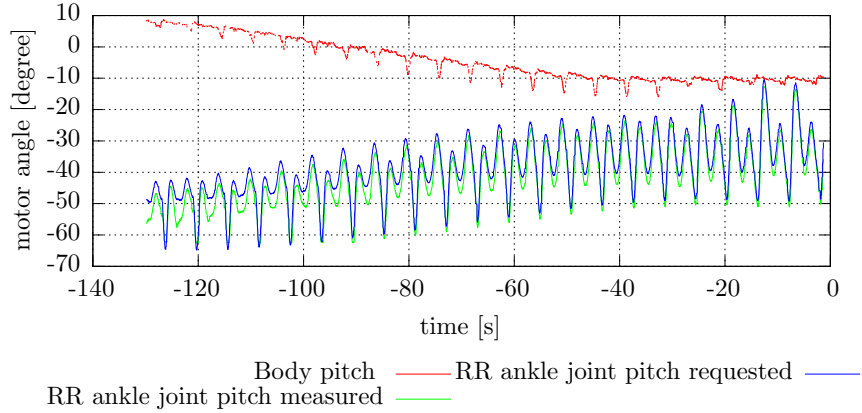


Figure 27: Walking up and down a slope with 10° and active local control loop. In the beginning while walking uphill a deviation of up to 10° is permitted, the context changes while the robot performs a turning motion on the slope and thus does the behavior of the local control loop.

more and more inefficient while walking downhill, as shown in Table 8 and Table 9. As mentioned before, it is possible to remedy the big disadvantage of low-level control and to provide a context awareness up to a certain point. As for all experiments, also during this run, no user input or any other external influence was given to the robot except when to start and stop the turning motion. While walking uphill, the local control loop was active based on the given context, consisting of the walking mode, the progress of each phase of the walking cycle and the incline measured by the IMU. During and after the turning motion the context information sent to the lower control changes the behavioral effect, as it can be seen in the plot starting at second 83. A deviation from the desired trajectory will after a certain point no longer be allowed, the local control loop configuration is autonomously changed from *setup 4* to *setup 2*.

4.4.4 Shifting the Center of Mass during Walking

The robot changes its Center of Mass (CoM) during walking constantly in form of an eight (indicated in Fig. 18 by the ZMP shifting) by changing its body posture. By using the forward kinematics, measured motor angles, and weight distribution, the measured 3D-trajectory of the CoM is visualized in the following section. Like in a robotic manipulator, in Charlie the hand and feet are defined as end-effector and the body as base.

The robot is controlling its CoM according to the perceived ZMP, leading to an actively adapting posture during walking along inclined slopes (see Table 10). To achieve reliable and repeatable results, the following data is recorded on a freely adjustable slope. Each inclination from -20° to 20° was tested at least four times with a minimum covered distance of 2 m.

Table 10: The table shows the CoM displacement on the x-axis in body coordinates in different inclines. The value is given at the intersection point of the eight-figured center of mass shifting while walking. The data presented bases on four runs with at least 10 step-cycles, thus 40 repetitions.

Incline in $^{\circ}$	Displacement of the CoM in <i>Setup 1</i> in mm	Displacement of the CoM in <i>Setup 2</i> in mm	Displacement of the CoM in <i>Setup 4</i> in mm
20	-75.1 (± 0.2)	-68.9 (± 0.5)	-68.3 (± 0.2)
15	-85.6 (± 0.7)	-80.6 (± 0.3)	-79.6 (± 0.2)
10	-96.2 (± 0.2)	-92.0 (± 0.2)	-92.8 (± 0.3)
5	-109.0 (± 0.2)	-105.7 (± 0.1)	-106.2 (± 0.3)
0	-122.6 (± 0.3)	-120.0 (± 0.4)	-120.8 (± 0.2)
-5	-135.9 (± 0.1)	-134.5 (± 0.2)	-134.1 (± 0.2)
-10	-148.6 (± 1.4)	-149.1 (± 0.1)	-149.2 (± 0.1)
-15	-160.0 (± 0.4)	-161.4 (± 0.3)	-160.1 (± 0.3)
-20	-170.7 (± 0.6)	-173.2 (± 0.2)	-171.7 (± 0.7)

The numbers in the parentheses indicate the deviation from the average over four runs. When walking on a flat surface, the center of the shifting curve is around -122 mm along the x-axis. Walking up a slope, the body is leaning forward to keep the CoM projected onto the plane within the support polygon. If the system walks downhill, the CoM is shifted backwards. It can be seen that the shift is nearly linear depending on the slope.

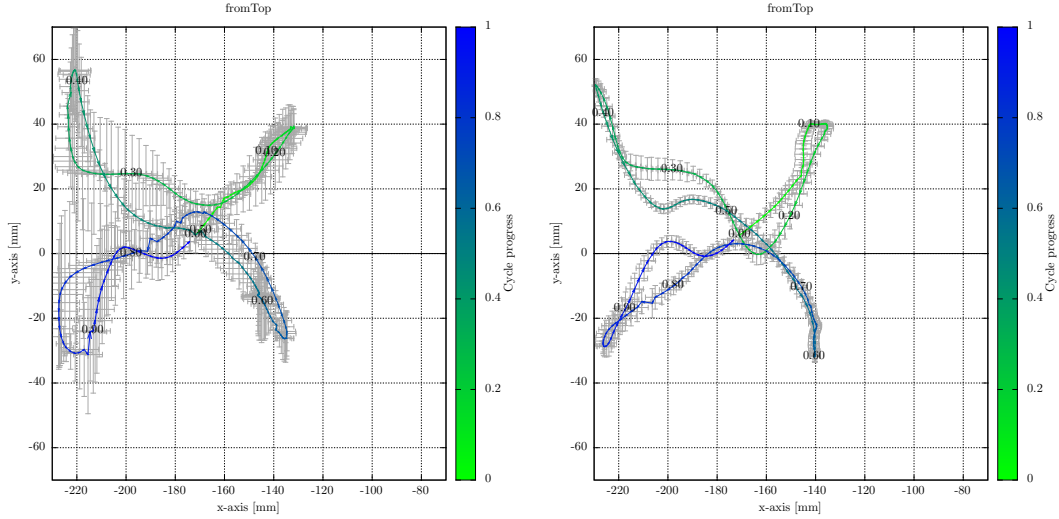
Between 0.2 and 0.7 in the cycle progress, the CoM reaches its maximum height in z-direction. This is caused by the swing-phase of the two heavier rear legs (see also Figure 11).

The investigated setups introduce additional movements of the spine or an adaptive behaviour in the ankle joints. The actual weight distribution of the overall system is not influenced very strongly by these. This is reflected in a similar trajectory of the CoM across the experiments.

In the following, the shifting of the zero moment point of the system in the different slopes is described. For better illustration, only the top view on the system is shown in the following figures. The mean deviation of the executed trajectory over multiple walking cycles of the run is visualized by gray bars, while the advance in the cycle progress is indicated by changing color as well as additional numbers attached to the curve.

Comparing the plots from Fig. 28(a) to Fig. 28(b), it can be seen that the pattern of the ZMP -shift in the *setup 4* does not change much. This result is due to the fact that the local control loop reduces the moments in the beginning of the stance-phase and thus a better form closure between sole and ground can be achieved, which leads to increased friction/traction.

As with the center of mass shifting, a considerably smaller mean deviation can be observed in *setup 4* with respect to *setup 2*. This behaviour is similar for all positive inclines and negative inclines up to -10° . In



(a) Shifting the zero moment point while walking in a slope with 20° (*setup 2*) (b) Shifting the zero moment point while walking in a slope with 20° (*setup 4*)

Figure 28: Shifting the zero moment point while walking in different slopes

slopes with -15° and -20° the mean deviation in *setup 4* approaches the deviation of the experiments in *setup 2*. If the local control loop is active, the robot center of mass moves in a consistent manner with only a few outliers. The lower outliers indicate a more stable behavior of the robot and therefore the controller output is decreased. Thus, the motors make less unnecessary motions, which is why even the reduced power consumption can be explained as soon as the local control loop is active. In comparison with the CoM trajectories, the ZMP trajectories are much more erratic. Because of the short-term accelerations resulting from discrete posture changes, IMU sensor noise and other sources the ZMP always moves around the desired trajectory.

A lower standard deviation means that the optimal and predicted CoM trajectory is met more precisely, which is a favourable effect. A more stable behavior of the robot is the consequence.

4.5 Conclusion of Four-Legged Walking Experiments

In the following the so far the experimentally achieved results will be summarized and the deficits and benefits will be pointed out. It can be stated that the robots morphology is very well suited to deal with all tested different terrains. The experiments within the laboratory and outside in different substrates, such as lawn or in the gravel field as well as on the slope with an adjustable inclination of -20° to 20° were necessary to evaluate experimentally the functionality e.g. of the active artificial spine or the local control loop in different circumstances.

It is to emphasize that the local control loop, in addition to lowering the acting torques in the system, reduces tenseness between the legs (cf. Fig. 23) and the body and thus reduces the overall current consumption even though additional movement by the ankle joint is introduced. However, much more important is the fact that the local control loop enables the robot to cope with environments, which, without active local control loop, it would not be able to overcome (as shown in the gravel field). An initial drawback of the local control loop was shown while walking down-hill. Even though the robot is able to walk down in a stable manner, for the sake of the overall current consumption due to the introduction of context-based adaptation the initial drawback could be dissolved. The introduced active spine allows a reduction of maximum needed speed of each individual joint within the legs while walking. The robot's hardware is exposed to less mechanical stress, shorter step cycles can be performed and thus the walking speed can be increased.

5 Bipedal Walking Experiments and Results

A defining feature of a hominid robot is the ability to walk bipedally and quadrupedally. This presents an opportunity to investigate the transferability of motion patterns or control schemes from four to two-legged walking or vice versa. One of the questions is, if a certain four-legged motion sequence may also serve for bipedal walking in direct or modified form? Answers to questions, which are in line with this one could provide clues for understanding the evolution of bipedal locomotion. Based on performed experiments, distinctive characteristics in joint angles were found, which are similar for bipedal and quadrupedal locomotion. With that said, one has to keep in mind that the robot was modeled after chimpanzees, which occasionally walk upright, but their main locomotion mode still remains on four legs. Thus, Charlie's morphology differs from systems which can be classified as humanoid robots.

5.1 Posture Transition

As stated before, due to the desire to realize several locomotion modes, the system was designed to be able to move on four legs but should also have the capabilities for bipedal walking. Besides walking, a two-legged posture makes it possible to pick up objects, freeing the front legs to use tools, manipulate objects, or carrying a certain payload.

Before the robot is able to realize such behaviors, it has to move itself in an adequate pose. Therefore, a transition between these two basic postures has been realized. Figure 29 shows the stand-up motion, a transition from a four-legged posture into an upright posture. The complete sequence needs about 15 s time,

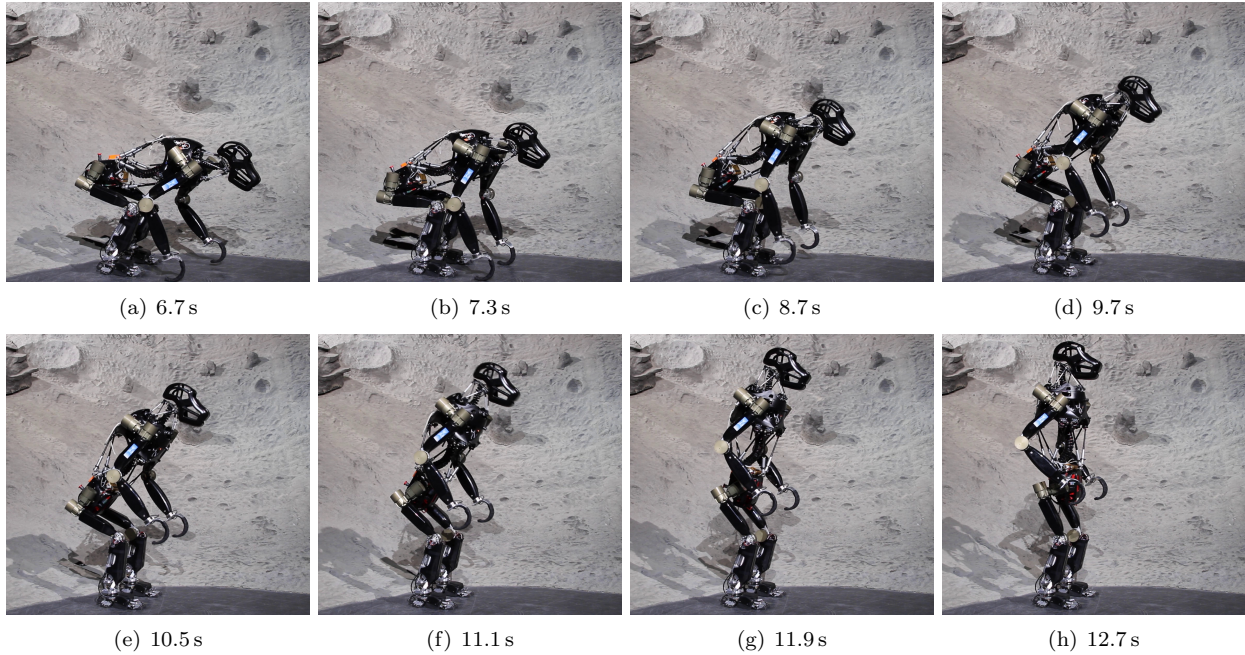


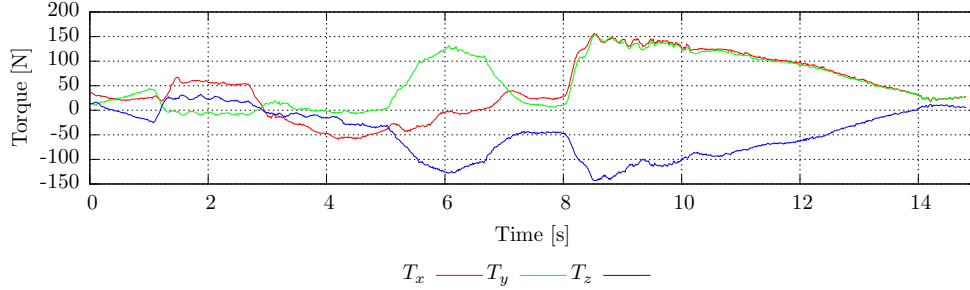
Figure 29: Transition from a four-legged into a two-legged posture

the actual stand-up motion needs less than 5 s. This includes two steps of the front legs to shift the CoM closer to the rear legs. As it can be seen in the picture sequence, the transition takes place without external assistance. Due to its multi-point-contact feet (MPCF) the robot is stable at all times.

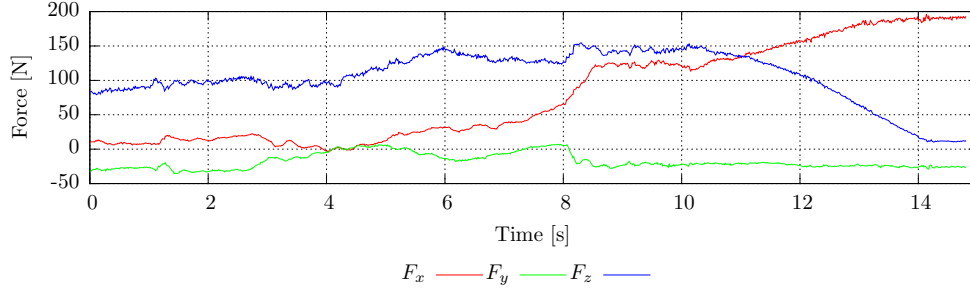
As for walking, during the stand-up motion the desired joint angles are interpolated on joint level. While standing on two legs, the overall power consumption for all joints together is as low as 50 mA at 48 V (2.4 W). For comparison, the four-legged posture consumes about 4.5 W. Presumably the more bent legs result in greater torques at knee and hip/shoulder joints, whereas the rear legs are more stretched out when standing erectly.

Figure 30(a) shows the applied torque to the spine during posture transition. In the beginning of the line graph, the steps of the front legs and a CoM-shifting can be seen. At 8 s, the CoM is between the rear feet and the front feet become load free. This means, the upper body weight including front limbs is now affecting the spine force and torque measurement. The more the robot gets to its upright posture, the less torque affects the body parts.

Figure 30(b) shows the sum of the measured forces of both rear feet in the body frame. The lower force value in the beginning is due to a weight distribution on all four legs. Around second eight, the front feet become more and more load free and meanwhile the rear legs have to carry all weight (as indicated by the blue line).



(a) Applied torque in the spine



(b) Measured force in both rear feet

Figure 30: Selected force and torque plots during the transition from a four-legged into a two-legged posture within the body frame

At the end, the robot stands on two legs, so the force value has to double (force x in the figure). For a better demonstration, the figure shows that force x and force z exchange their position during transition. During the transition, the body coordinate system rotates nearly 90° around the y-axis. As mentioned earlier, the body frame is defined by the axis along hip and shoulder. The stand up behavior effects the body coordinate system in a way that the x-axis points now in z direction and thus along the gravity direction. The z-axis on the other hand points in negative x-axis direction.

5.2 Bipedal Walking

Once the robot stands upright, a bipedal walking is possible to achieve. As with many humanoid robots, in Charlie a ZMP based control approach is implemented, whereas the entire body mass is considered as a single point. Currently, the robot is able to walk stable with a walking pattern in which the feet are moved fast from back to front (gait cycle time about 1.6s). While walking with a slower, more static, walking pattern (comparable with the four-legged locomotion), external assistance is needed to stabilize the robot. It can be stated that quadrupedal locomotion is significantly more stable due to a larger support polygon. To improve the balance of a humanoid robot, different approaches have been explored in various working groups. These approaches include railings (Harada et al., 2004), trekking sticks (Khatib and Chung, 2014),

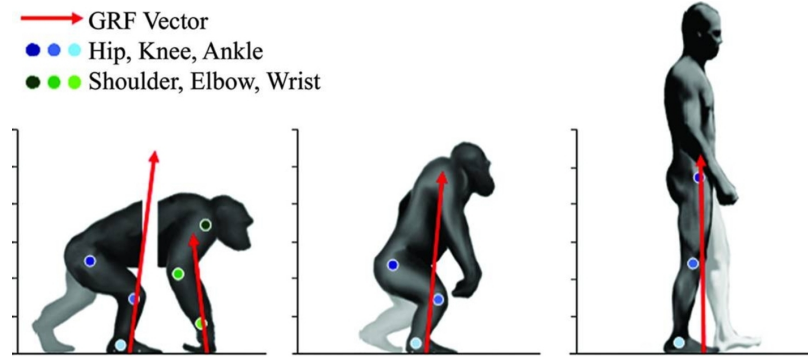


Figure 31: Comparison of walking postures in chimpanzees and humans. GRF stands for ground reaction force. Figure from (Sockol et al., 2007)

or canes (Kobayashi et al., 2013). In contrast to other studies (Kajita et al., 2003), the arms of the robot cannot be used to compensate for the moments of inertia of the feet, since they do not have enough weight for this purpose. As mentioned before, Charlie's morphology differs from humanoid robots. This is also reflected in the walking pattern. Sockol analyzed bipedal walking in chimpanzees and compared walking mechanics in chimpanzees and humans (Sockol et al., 2007). Figure 31 shows the differences between both, the ape-like and the human bipedal posture. In Charlie a bent-hip - bent-knee posture while walking is used (see center image in Fig. 31). Keeping the hip and knee joints bent requires more energy in these two joints, but it is a lot more stable than walking bipedal like a human.

Since the robot has a stiff claw as hand, an approach was chosen in which no modification of the robot's hardware is needed. In the first phase, the robot's left arm reaches out to get the needed support by a handrail, ballet barres, or a human. A walking support provided by a handrail or ballet barres contains the danger of tilting the bar in the hook-shaped hand. The data provided in the following was recorded while performing a walking supported by a human. During the two-legged locomotion experiments, potential internal sources of error were identified and could be tackled individually allowing Charlie to perform a slower, more static bipedal locomotion. Fig. 32 shows the robot walking on the outside robot test track. As for the slope experiments, due to uneven ground, the walking experiments were performed again on an inside test track to gain data that is repeatable and significant.

The data shown in Fig. 33 compares the joint angles of the described four-leg locomotion (red line), the dynamic bipedal gait without assistance (blue line), and the more static bipedal gait, where assistance is needed (green line). Figure 33(e) shows measured absolute force and torque data of the left arm while walking; in other words, the support needed for a slower and more static walking.

Two support phases can be seen, one for each leg swing-phase. Between 0.1 and 0.2 as well as between 0.6

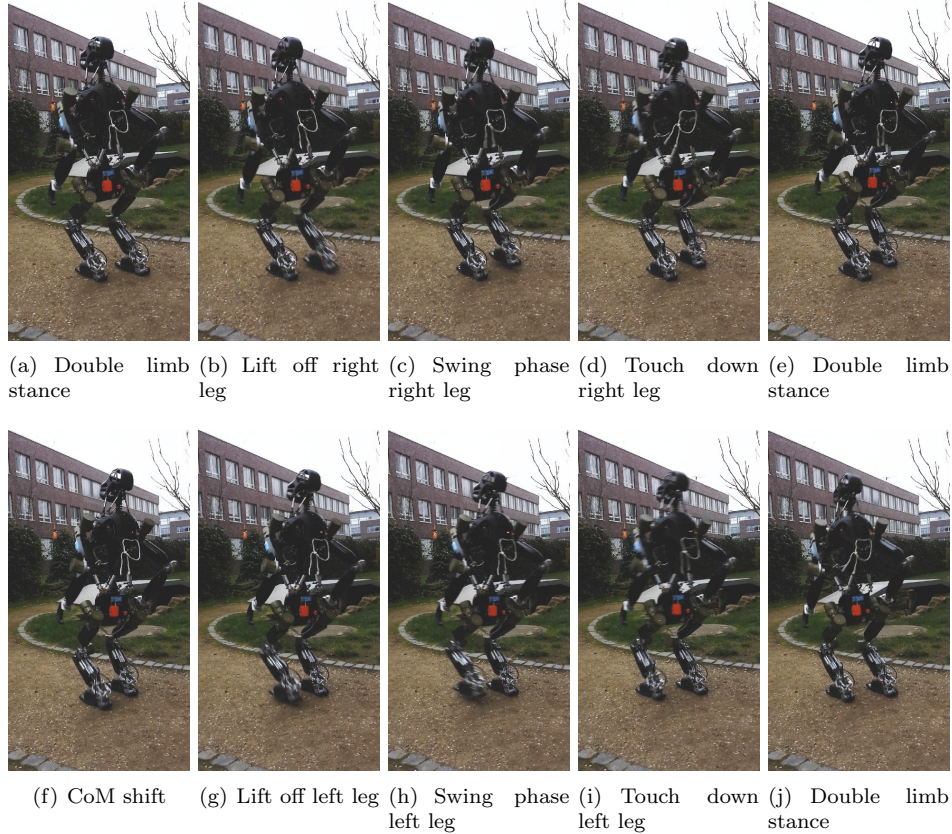


Figure 32: Two-legged walking

and 0.7 the ZMP is shifted from the left to the right or vice visa. In these double stance-phase both feet are on the ground.

During the swing-phase, in sum a force of less than 20 N is necessary to stabilize the robot. This also includes shear forces. If only the applied force in y-direction is taken into account, a maximum of -7 N (the robot pulls on the handle) and 15 N (pushing the handle) is needed.

To be able to compare bipedal and quadrupedal walking, both have to use an equal parameter set. *Speed setting ramp* seems to be a decent parameter set, since the stride length is also suitable for bipedal walking. Due to the given support, the feet are lifted only 40 mm, not 100 mm like listed in the quadrupedal experiment. Further parameters are equal to the one described in the experiment section. The data was recorded while walking on *terrain 1* using *setup 1*. For the stable bipedal walking, individual parameters became adapted. The gait cycle time is set to 1.6s, the step length is set to 100 mm, the ZMP is shifted 30 mm to the front, the balance controller output is reduced by 70%, and no body pitch and roll motions are allowed.

In the following, walking pattern A indicates the quadrupedal gait, walking pattern B bipedal walking with

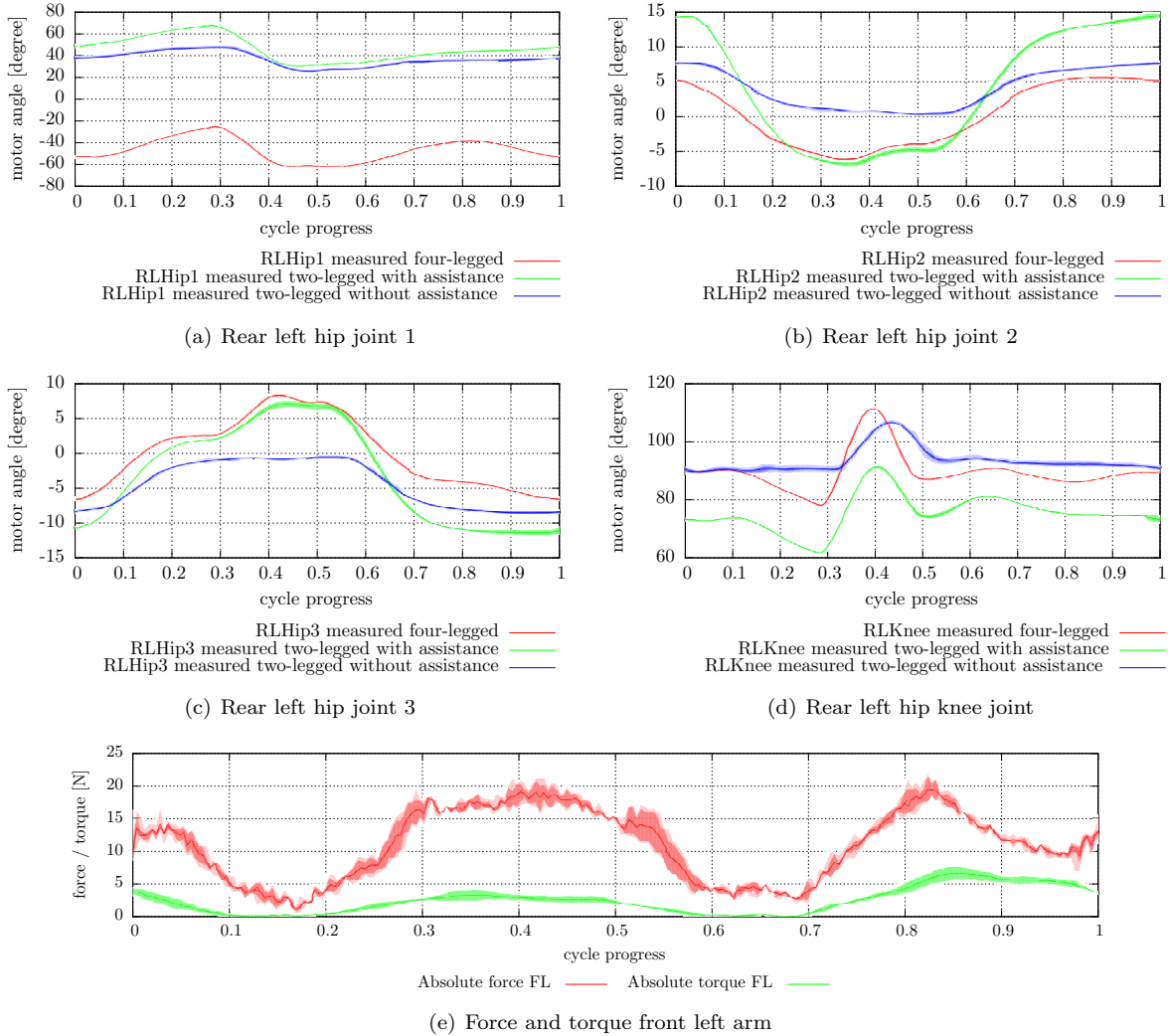


Figure 33: (a) - (d) show selected angle plots while walking quadrupedal and bipedal. In (e) the force and torque of the front left arm are displayed, showing the needed support while walking bipedal with assistance.

assistance and walking pattern C bipedal walking without external assistance. It can be seen clearly for all joints that the trajectory for walking pattern A and B are similar in shape, but not identical. In contrast to walking pattern B, walking pattern A shows a slight undulation in the beginning of Fig. 33(a). The amplitude range, however, does not differ significantly between walking pattern A and B, but for pattern C. This is due to the reduced gait cycle time.

On the contrary to the first hip joint, the amplitude in Fig. 33(b) and Fig. 33(c) differs of about 10° for hip joint two and 5° for hip joint three between walking pattern A and B. These joints mainly used for lateral movements, e.g. to walk curves or to shift the ZMP. During four-legged walking, shifts of the body are considerably smaller than during two-legged walking because of the larger support polygons spanned by at least three legs. For walking pattern C the shifting is reduced to 30%, so a lower amplitude is expected.

The knee joint (Fig. 33(d)) as well as hip joint one shows a shifted range of values for walking pattern B and C, which is due to the different posture of the robot. Still, the shape of the curve for walking pattern B matches the one from walking pattern A. It can be seen that the knee trajectory from walking pattern C displays a similar curve shape compared to walking pattern B, albeit in weakened form.

5.3 Two-Legged Walking with Active Local Control Loop

After presenting a comparison of the joint trajectories for the four-legged and two-legged locomotion in the previous chapter, in the following is examined whether the local control loop can be used directly or in a modified form for two-legged walking. A detailed description of the local control loop including the parameter-set can be found in (Kuehn et al., 2014)

The first experiments showed clearly that the robot is not able to walk, if the local control loop parameters are not adjusted to this motion mode. As for the four-legged walking, the local control responds to the measured moments, which are now increased due to the posture change. The nearly instantaneous movement is in response to the stimulus intensity, which in turn means that the foot cannot provide the required stability in the beginning of the stance-phase and Charlie starts tipping over.

In order to adapt local control loop behavior to this motion mode, experiments were performed to determine appropriate parameters empirically. The compliance of the foot depends on the gait cycle progress. In addition, a threshold can be set to adapt the stiffness of the local control loop. The larger the threshold the smaller the movement of the foot. This threshold of course affects as well the intensity of the foot deflection based on the acting torques. A reduction however is logical, as a pitch movement in the foot of up to 20° does not make sense for bipedal walking.

Figure 34 shows the foot deflection while walking two-legged with and without active local control loop. Compared to the active local control loop in four-legged walking it can be seen that a maximal adaption of 4° takes place. The measured curves follow strongly the desired trajectories without allowing large outliers. For bipedal walking, a larger deflection results in a reduction of the robots stability and thus reduces its ability to walk without support.

5.4 Conclusion of Two-Legged Walking Experiments

To conclude, it can be said that Charlies morphology and design allows a stable transition between the fundamentally different postures in both directions. The shown data suggests that at least for this robotic

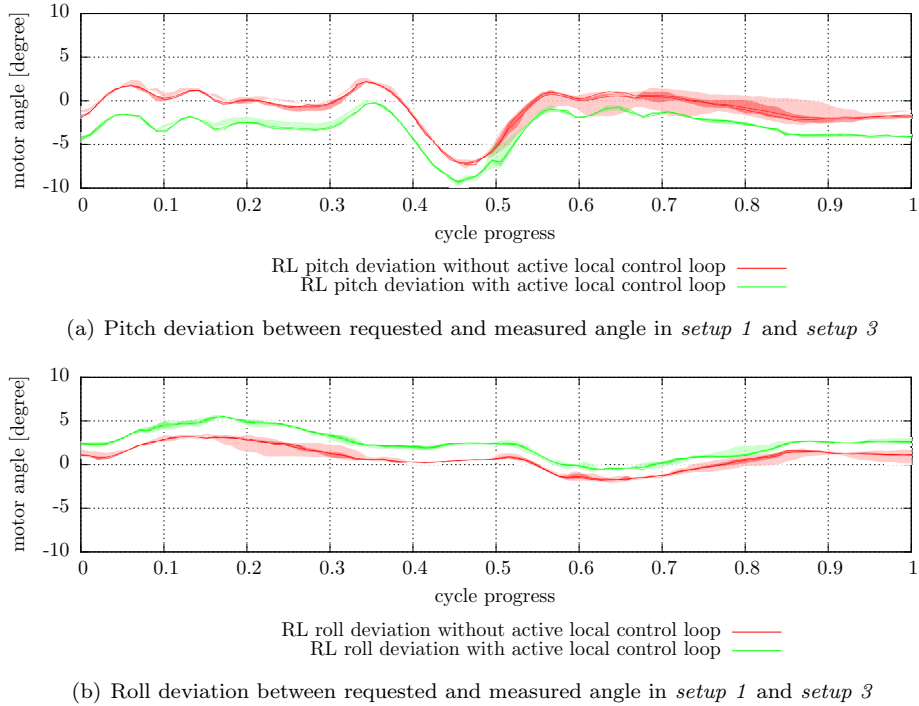


Figure 34: Differences of the measured roll and pitch angle in the rear left ankle joint in *setup 1* (without active local control loop) and *setup 3* (active local control loop) on *terrain 1*: Laboratory floor

system, similar joint (and so cartesian) trajectories can be used for both, the quadrupedal and bipedal walking with support. Through adaptations on the parameter set, the robot is able to perform bipedal locomotion. The slight adaptations of the trajectories in amplitude and phase were identified, with which the robot was then able to walk. A similarity of the trajectories can be observed in this case as well, although not as distinctive as in the supported walking.

6 Conclusion and Outlook

In this paper, a hominid multi-locomotion robot including two major subsystems, sensory multi-point-contact feet and artificial spine, is presented. Besides the robot, the usage of an implemented local control loop is shown, which increases the robot's stability successfully while dealing with different environments. The experiments show that the robot Charlie is able to walk on four legs on unstructured soils, climbs slopes of up to $\pm 20^\circ$ up and down, perform a motion to stand only on its rear feet, and is also able to walk bipedal. The last chapter closes with a comparison of joint trajectories both for the quadrupedal and bipedal walking patterns.

The robot Charlie has been build with the intend to create a light-weight system with intelligent substructures. The structures designed and built are as self-contained as possible with regard to sensing, sensor preprocessing, control and communication. To increase the mobility towards a multi-locomotion system (i.e. providing the means to walk quadrupedal or bipedal), the rigid connection between the front and rear body has been replaced by an actuated spinal column with six degrees of freedom. Another step towards bipedal walking was the development of more advanced rear feet. Multi-point-contact feet can improve traction control in quadrupedal walking and allow bipedal walking. To make use of these advantages, the lower legs of the robotic system were developed and integrated with an actuated ankle joint, an attached MPCF-structure and a set of sensors including appropriate electronics.

Due to the embedded sensors and electronics, the implementation of a local control loop became feasible. Although the local control loop modifies the desired joint angles coming from the walking pattern generator, undesired side-effects have not been observed. The additional behavior allows the robot to cope with uneven ground in a four-legged posture, without the need to search for a working parameter set experimentally or by using machine learning. The local control loop lead to an improvement regarding the ability of the robot to cover unstructured environment. Without the local control loop, locomotion in such environments would not have been even possible.

Clearly, the robot has by no means reached the end of its development. There were some lessons learned in the design and testing phase with the prototype. The leg structure and the ankle joints itself have to become stiffer, to allow a non-dynamic humanoid walking. Later revisions of the robot might also extent the existing structure with dexterous manipulation devices expanding the range of possible application areas. For example, the hooks on the front legs can become active grippers. Current work is to take more of the available sensor and preprocessed data into account, allowing the system to be used in even more unstructured environments. Other locomotion modes, like trot and cross gait or highly dynamic bipedal gaits, are going to be implemented to gain further insight regarding the reuse of functionality. In addition to that, high-level control like self-localization and path planning can be implemented to increase the robots autonomy. For this purpose, the integration of further sensory equipment within the head is intended. This includes stereoscopic visual sensing and processing capabilities.

Distributed computation is applied in various cases to the robot which reduces requirements regarding central processing power. Beyond that, local sensor processing is reducing the amount of data needed to be sent to a higher control level. Additional force-based control approaches – in joint or Cartesian space – could be integrated into the system to mitigate unwanted effects in unstructured terrain or during dynamic

locomotion. If possible, the distributed architecture should be further exploited to reduce the computational load on the central control board.

Due to the 6-DoF force/torque sensor functionality, load applied to the spine while interacting with the environment can be measured. Thus it is possible, for example, to fuse spine and feet sensors to verify a detected touchdown or apply virtual springs to reduce the influence of shocks. The design of the artificial spine simplifies integration of mechanical springs and dampers by modifying the existing rods, which could be embedded to change the dynamic behavior of the system.

Acknowledgement

We would like to thank all members of the DFKI Bremen Robotics Innovation Center (RIC) and Robotics Lab of the University of Bremen which supported us in this work.

This work was performed within the Intelligent Structures for Mobile Robots (*iStruct*) and VIPE project. The both projects are funded by the Space Agency of the German Aerospace Center with federal funds of the Federal Ministry of Economics and Technology (BMW) in accordance with the parliamentary resolution of the German Parliament, grant no. 50RA1013 and grant no. 50RA1014 for *iStruct* and 50NA1516 for VIPE.

References

- Acaccia, G., Bruzzone, L., Michelini, R., Molfino, R., and Razzoli, R. (2000). A tethered climbing robot for firming up high-steepness rocky walls. In *Proc. of the 6th IAS Intl. Conf. on Intelligent Autonomous Systems*.
- Albiez, J., Dillmann, R., and Hinckel, T. (2005). Reactive foot-control for quadruped walking. In *3rd International Symposium on Adaptive Motion in Animals and Machines*.
- Bartsch, S., Birnschein, T., Roemmermann, M., Hilljegerdes, J., Kuehn, D., and Kirchner, F. (2012). Development of the six-legged walking and climbing robot spaceclimber. *Journal of Field Robotics*, Volume 29, Issue 3, Special Issue on Space Robotics(Part 1):506–532.
- Bluethmann, W., Ambrose, R., Diftler, M., Askew, S., Huber, E., Goza, M., Rehnmark, F., Lovchik, C., and Magruder, D. (2003). Robonaut: A robot designed to work with humans in space. *Autonomous Robots*, 14(2-3):179–197.

- Briggs, R., Lee, J., Haberland, M., and Kim, S. (2012). Tails in biomimetic design: Analysis, simulation, and experiment. In *Intelligent Robots and Systems (IROS), 2012 IEEE/RSJ International Conference on*, pages 1473–1480.
- Buschmann, T., Lohmeier, S., and Ulbrich, H. (2009). Humanoid robot lola: Design and walking control. *Journal of Physiology-Paris*, 103(3-5):141 – 148.
- Crespi, A., Karakasiliotis, K., Guignard, A., and Ijspeert, A. J. (2013). Salamandra Robotica II: An Amphibious Robot to Study Salamander-Like Swimming and Walking Gaits. *IEEE Transactions on Robotics*, 29(2):308–320.
- Crompton, R. H. (1996). Inertial properties of primates: New techniques for laboratory and field studies of locomotion. In *American Journal of Physical Anthropology* 99, 547-570.
- Csonka, P. and Waldron, K. (2011). A brief history of legged robotics. In Ceccarelli, M., editor, *Technology Developments: the Role of Mechanism and Machine Science and IFToMM*, volume 1 of *Mechanisms and Machine Science*, pages 59–73. Springer Netherlands.
- Diftler, M., Ahlstrom, T., Ambrose, R., Radford, N., Joyce, C., De La Pena, N., Parsons, A., and Noblitt, A. (2012). Robonaut 2 2014; initial activities on-board the iss. In *Aerospace Conference, 2012 IEEE*, pages 1–12.
- Espenschied, K. S., Quinn, R. D., Beer, R. D., and Chiel, H. J. (1996). Biologically based distributed control and local reflexes improve rough terrain locomotion in a hexapod robot. *Robotics and Autonomous Systems*, 18:59 – 64.
- Fallon, M., Kuindersma, S., Karumanchi, S., Antone, M., Schneider, T., Dai, H., D’Arpino, C. P., Deits, R., DiCicco, M., Fourie, D., Koolen, T., Marion, P., Posa, M., Valenzuela, A., Yu, K., Shah, J., Iagnemma, K., Tedrake, R., and Teller., S. (2014). An architecture for online affordance-based perception and whole-body planning. Technical report, MIT CSAIL.
- Fondahl, K., Kuehn, D., Beinersdorf, F., Bernhard, F., Grimminger, F., Schilling, M., Stark, T., and Kirchner, F. (2012). An adaptive sensor foot for a bipedal and quadrupedal robot. In *Proceedings of IEEE International Conference on Biomedical Robotics and Biomechatronics*.
- Harada, K., Hirukawa, H., Kanehiro, F., Fujiwara, K., Kaneko, K., Kajita, S., and Nakamura, M. (2004). Dynamical balance of a humanoid robot grasping an environment. In *Proceedings of the IEEE/RSJ International Conference on Intelligent Robots and Systems*, volume 2, pages 1167–1173 vol.2.

- Hashimoto, K., Sugahara, Y., Lim, H. K., and Takanishi, A. (2006). New biped foot system adaptable to uneven terrain. *Journal of Robotics and Mechatronics*, 18 No. 3:271–277.
- Hawkes, E., Ulmen, J., Esparza, N., and Cutkosky, M. (2011). Scaling walls: Applying dry adhesives to the real world. In *Intelligent Robots and Systems (IROS), 2011 IEEE/RSJ International Conference on*, pages 5100–5106. IEEE.
- Hilljegerdes, J., Spenneberg, D., and Kirchner, F. (2005). The construction of the four legged prototype robot ARAMIES. In *Proceedings of the 8th International Conference on Climbing and Walking Robots (CLAWAR 2005)*, pages 335–342, London, UK.
- Hinojosa, W. M., Tsagarakis, N. G., Metta, G., Becchi, F., Sandini, G., and Caldwell, D. (2006). Performance assessment of a 3 dof differential based waist joint for the “icub” baby humanoid robot. In *15th IEEE International Symposium on Robot and Human Interactive Communication*, pages 195–201. Hatfield, United Kingdom.
- Hirose, S., Yoneda, K., and Tsukagoshi, H. (1997). Titan vii: Quadruped walking and manipulating robot on a steep slope. In *Proceedings of the 1997 IEEE International Conference on Robotics and Automation, Albuquerque, New Mexico*.
- Holland, O. and Knight, R. (2006). The anthropomimetic principle. In *Proceedings of the AISB06 Symposium on Biologically Inspired Robotics*.
- Hutter, M., Gehring, C., Bloesch, M., Hoepffinger, M. A., Remy, C. D., and Siegwart, R. (2012). Starleth: A compliant quadrupedal robot for fast, efficient, and versatile locomotion. In *Climbing and Walking Robots (CLAWAR)*.
- Jantsch, M., Wittmeier, S., and Knoll, A. (2010). Distributed control for an anthropomimetic robot. In *Intelligent Robots and Systems (IROS), 2010 IEEE/RSJ International Conference on*, pages 5466–5471.
- Ji, L. Y. and Kirchner, F. (2013). Reducing intersample ripple of actuator in multirate environment by a joint space interpolator. In *The 6th IFAC Symposium on Mechatronic Systems. IFAC Symposium on Mechatronic Systems (Mechatronics-2013), 6th, April 10-12, Hangzhou, China*.
- Kajima, H., Doi, M., Hasegawa, Y., and Fukuda, T. (2003). Study on brachiation controller for the multi-locomotion robot -redesigning behavior controllers. In *Proceedings of the 2003 IEEE RSJ*.
- Kajita, S., Kanehiro, F., Kaneko, K., Fujiwara, K., Harada, K., Yokoi, K., and Hirukawa, H. (2003). Resolved momentum control: humanoid motion planning based on the linear and angular momentum. In *Intel-*

- ligent Robots and Systems, 2003. (IROS 2003). Proceedings. 2003 IEEE/RSJ International Conference on*, volume 2, pages 1644–1650 vol.2.
- Khatib, O. and Chung, S. Y. (2014). Suprapeds: Humanoid contact-supported locomotion for 3d unstructured environments. In *IEEE International Conference on Robotics and Automation (ICRA)*, pages 1–6.
- Kirchner, F., Spenneberg, D., and Linnemann, R. (2002). A biologically inspired approach towards robust real world locomotion in an 8-legged robot. In *J. Ayers, J. Davis, and A. Rudolph (Eds.), Neurotechnology for Biomimetic Robots. MIT-Press, MA, USA*.
- Kobayashi, T., Aoyama, T., Sobajima, M., Sekiyama, K., and Fukuda, T. (2013). Bipedal walking by humanoid robot with cane; preventive usage of cane based on impulse force. In *Micro-NanoMechatronics and Human Science (MHS), 2013 International Symposium on*, pages 1–6.
- Kuehn, D., Beinersdorf, F., Bernhard, F., Fondahl, K., Schilling, M., Simnofske, M., Stark, T., and Kirchner, F. (2012). Active spine and feet with increased sensing capabilities for walking robots. In *International Symposium on Artificial Intelligence, Robotics and Automation in Space (iSAIRAS-12)*. September 4-6, Turin, Italy.
- Kuehn, D., Beinersdorf, F., Simnofske, M., Bernhard, F., and Kirchner, F. (2013). Towards an active spine for mobile robots. In *3rd IFToMM International Symposium on Robotics and Mechatronics. International Symposium on Robotics and Mechatronics (ISRM-2013), October 2-4, Singapore, Singapore*. o.A.
- Kuehn, D., Bernhard, F., Burchardt, A., Schilling, M., Stark, T., Zenzes, M., and Kirchner, F. (2014). Distributed computation in a quadrupedal robotic system. *International Journal of Advanced Robotic Systems*, 11.
- Lian, F.-L., Moyne, J., and Tilbury, D. (2002). Network design consideration for distributed control systems. *Control Systems Technology, IEEE Transactions on*, 10(2):297–307.
- Luo, J., Zhang, Y., Hauser, K., Park, H., Paldhe, M., Lee, C., Grey, M., Stilman, M., Oh, J. H., Lee, J., Kim, I., and Oh, P. (2014). Robust ladder-climbing with a humanoid robot with application to the darpa robotics challenge. In *Robotics and Automation (ICRA), 2014 IEEE International Conference on*, pages 2792–2798.
- McGhee, R. and Frank, A. (1968). On the stability properties of quadruped creeping gaits. *Mathematical Biosciences*, 3:331–351.

- Mizuuchi, I., Tajima, R., Yoshikai, T., Sato, D., Nagashima, K., Inaba, M., Kuniyoshi, Y., and Inoue, H. (2002). The design and control of the flexible spine of a fully tendon-driven humanoid kenta. In *Intelligent Robots and Systems, 2002. IEEE/RSJ International Conference on*, volume 3, pages 2527 – 2532 vol.3.
- Murphy, M. P., Saunders, A., Moreira, C., Rizzi, A. A., and Raibert, M. (2011). The littledog robot. *The International Journal of Robotics Research*, 30(2):145–149.
- NASA.gov – Mini-RF (2010). Exploring the lunar poles. http://www.nasa.gov/mission_pages/Mini-RF/multimedia/feature_ice_like_deposits.html.
- Nelson, G., Saunders, A., Swilling, B., Bondaryk, J., Billings, D., Lee, C., Playter, R., and Raibert, M. (2012). petman: A humanoid robot for testing chemical protective clothing . *Journal of the Robotics Society of Japan*, 30:372–377.
- Ogura, Y., Aikawa, H., Kondo, H., Morishima, A., Lim, H.-O., and Takanishi, A. (2006). Development of a new humanoid robot wabian-2. In *in Proceedings of IEEE International Conference on Robotics and Automation*, pages 76–81.
- Or, J. (2013). Humanoids grow a spine: The effect of lateral spinal motion on the mechanical energy efficiency. *Robotics Automation Magazine, IEEE*, 20(2):71–81.
- Ott, C., Eiberger, O., Friedl, W., Bauml, B., Hillenbrand, U., Borst, C., Albu-Schaffer, A., Brunner, B., Hirschmuller, H., Kielhofer, S., Konietzschke, R., Suppa, M., Wimbock, T., Zacharias, F., and Hirzinger, G. (2006). A humanoid two-arm system for dexterous manipulation. In *Humanoid Robots, 2006 6th IEEE-RAS International Conference on*, pages 276–283.
- Raibert, M. H. (1986). *Legged robots that balance*. Massachusetts Institute of Technology, Cambridge, MA, USA.
- Sakagami, Y., Watanabe, R., Aoyama, C., Matsunaga, S., Higaki, N., and Fujimura, K. (2002). The intelligent ASIMO: System overview and integration. In *IEEE/RSJ International Conference on Intelligent Robots and Systems*, volume 3, pages 2478 – 2483.
- Santos, D., Heyneman, B., Kim, S., Esparza, N., and Cutkosky, M. R. (2008). Gecko-inspired climbing behaviors on vertical and overhanging surfaces. In *Proceedings of the IEEE International Conference on Robotics and Automation (ICRA)*.
- Simpson, W. A. (1994). PPP in HDLC-like framing. RFC 1662 (Standard).

- Sockol, M., Raichlen, D., and Pontzer, H. (2007). Chimpanzee locomotor energetics and the origin of human bipedalism. *Proceedings of the National Academy of Sciences*, 104(30):12265.
- Spenneberg, D. and Kirchner, F. (2000). Omnidirectional walking in an eight legged robot. In *International Symposium on Robotics and Automation (ISRA)*.
- Spenneberg, D. and Kirchner, F. (2007). *The Bio-Inspired SCORPION Robot: Design, Control & Lessons Learned*, chapter Climbing & Walking Robots, Towards New Applications, pages 197–218. I-Tech Education and Publishing, Wien, Austria. ISBN: 978-3-902613-16-5.
- Stentz, A., Herman, H., Kelly, A., Meyhofer, E., Haynes, G. C., Stager, D., Zajac, B., Bagnell, J. A., Brindza, J., Dellin, C., et al. (2015). Chimp, the cmu highly intelligent mobile platform. *Journal of Field Robotics*, 32(2):209–228.
- Stoica, A., Keymeulen, D., Csaszar, A., Gan, Q., Hidalgo, T., Moore, J., Newton, J., Sandoval, S., and Xu, J. (2005). Humanoids for lunar and planetary surface operations. In *Systems, Man and Cybernetics, 2005 IEEE International Conference on*, volume 3, pages 2649–2654. IEEE.
- Takeda, Y., Funabashi, H., and Ichimaru, H. (1997). Development of spatial in-parallel actuated manipulators with six degrees of freedom with high motion transmissibility. *JSME International Journal*, 40:299–308.
- Tokuda, K., Toda, T., Koji, Y., Konyo, M., Tadokoro, S., and Alain, P. (2003). Estimation of fragile ground by foot pressure sensor of legged robot. In *IEEE/ASME International Conference on Advanced Intelligent Mechatronics (AIM 2003)*, pages 447 – 453.
- Tsujita, K. and Miki, K. (2011). A study on trunk stiffness and gait stability in quadrupedal locomotion using musculoskeletal robot. In *Proceedings of the IEEE International Conference on Advanced Robotics*.
- Wooden, D., Malchano, M., Blankespoor, K., Howardy, A., Rizzi, A., and Raibert, M. (2010). Autonomous navigation for bigdog. In *Robotics and Automation (ICRA), 2010 IEEE International Conference on*, pages 4736–4741.